Z. Shen,
M. A. Abdelmoneum
J. L. Volakis

Fast Hybrid PO-MM Analysis of Large Axi-Symmetric Radomes

Science and Applied Technologies
21050 Califa St.
Woodland Hills, CA 91367-5103

April 1999

PROJECT INFORMATION

PROJECT TITLE: Dielectric Radome Simulation with Fast Algorithms

REPORT TITLE: Fast Hybrid PO-MM Analysis of Large Axi-Symmetric Radomes

U-M REPORT No.: 037821-1-T

CONTRACT
START DATE: September 1998
END DATE: September 1999

DATE: April 1999

SPONSOR: Dr. Odell Graham
Science and Applied Technologies
21050 Califa St.
Woodland Hills, CA 91367-5103
Phone: (818)887-0844 x107
Fax: (818)887-1447

SPONSOR
CONTRACT No.: P.O. SW01073

U-M PRINCIPAL
INVESTIGATOR: John L. Volakis
EECS Dept.
University of Michigan
1301 Beal Ave
Ann Arbor, MI 48109-2122
Phone: (313) 764-0500 FAX: (313) 647-2106
volakis@umich.edu
http://www-personal.engin.umich.edu/~volakis/

PROJECT PEOPLE: Z. Shen, M. A. Abdelmoneum and J.L. Volakis

Contents

1 Introduction

This report details the development of a new hybrid physical optics-moment method (PO-MM) formulation for analysis of nose-radome antennas. The radome is assumed to be a body of revolution (BOR) and this is taken into consideration to reduce the overall problem to a two-dimensional one by decomposing the antenna radiated fields into cylindrical modes used as the excitation on the dielectric radome.

The primary reason for considering a hybrid PO-MM implementation stems from our interest to modal very large radomes which are possibly 100λ long and $30 - 40\lambda$ wide at the back of the radome where the antenna aperture resides (see Fig. 1). For this analysis, the radome shell is assumed uniform but layered configurations can be readily incorporated . In combining the PO and MM technique for evaluating the transmission properties of the radome, the MM is employed to rigorously model the tip of the radome (up to $3 - 5\lambda$ long) and account for diffraction contributions.

The PO method (i.e. ray optics) is employed to compute the transmitted fields away from the tip region where multiple scattering and tip diffraction effects are not pronounced. Higher-order ray interactions can, however, be included in the PO implementation to account for multi-bounce effects within the radome cavity.

In combining the PO and MM, an equivalent current is computed on the radome surface based on the PO fields computed at the interior and exterior surfaces of the radome. These are subsequently used as excitation in the context of the MM along with the direct antenna fields to evaluate the equivalent MM surface currents. The final radiation pattern is then evaluated by integrating the electric and magnetic equivalent currents (both PO and MM currents) on the exterior surface of the radome.

The report is organized as follows. Section 2 gives a description for evaluating the aperture radiation on the radome interior surface near-zone fields. These near-zone field components are then decomposed into cylindrical modes to subsequently perform the BOR moment method implementation. Section 3 introduces the physical optics (PO) approximation for both electric and magnetic surface currents on the flatter radome surfaces. The hybrid BOR moment method formulation is presented in Section 4. Here PO currents for the PO-region are incorporated

into the surface integral equation as effective sources. Numerical examples and validations (including a very large radome of 100 wavelengths) are given in Section 5. Finally, Sections 6 and 7 describe the Fortran program that implements the hybrid PO-MM BOR. Sample geometry runs are included as examples in using the hybrid code to be referred to herein as ABOR (Antenna-BOR).

2 Near Field Computation and Decomposition

The geometry of the problem considered is illustrated in Figure 1. The radome is assumed to be axi-symmetric (body of revolution), but the curvature of the inner and outer surfaces can be completely arbitrary. The aperture antenna (reflector, horn, open waveguide etc.) is placed inside (as illustrated) and its pattern can be arbitrarily selected as well. In this development, a circular aperture antenna is assumed but this is an arbitrary selection. The governing equation and pictorial shape of a Von Karman radome are given in Appendix A.

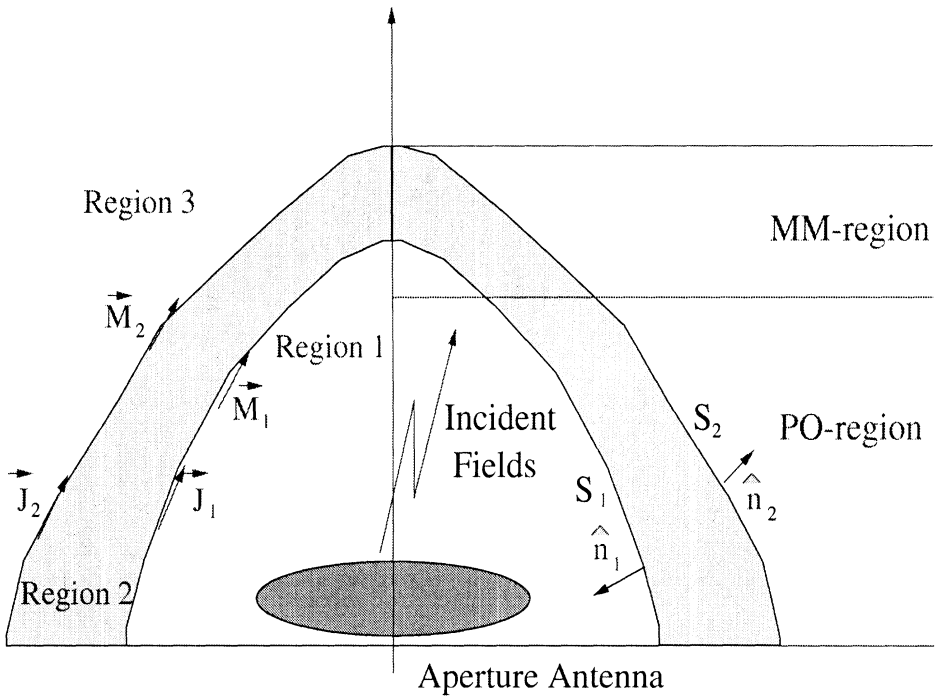

Figure 1: Geometry of the problem considered.

The circular aperture antenna is separately shown in Figure 2, with its corresponding coordinate system.

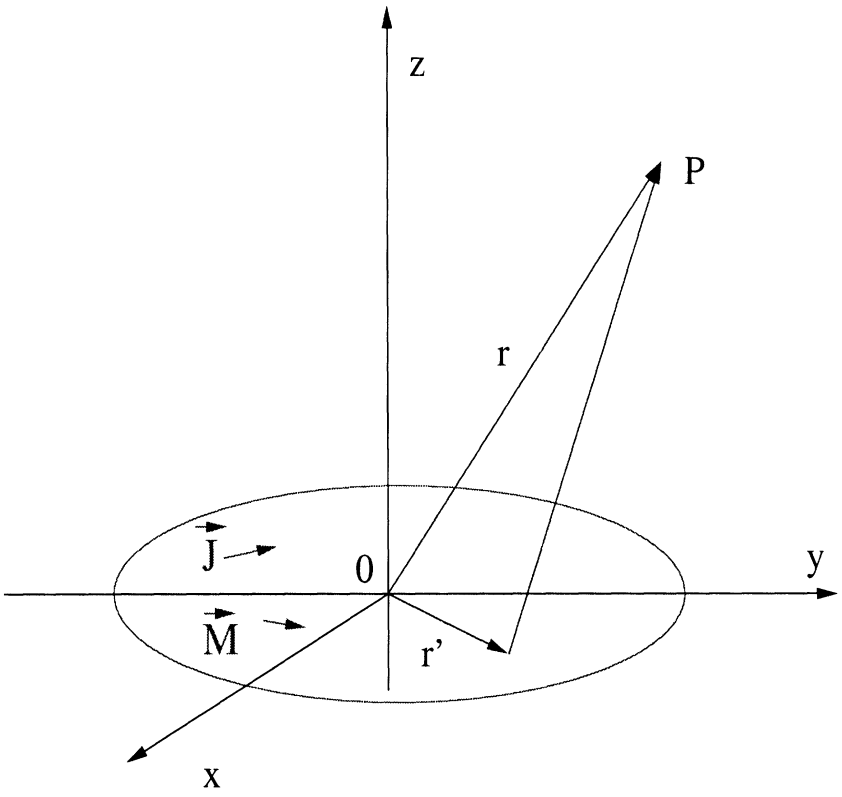

Figure 2: Circular aperture antenna

2.1 Near-Zone Field

Before proceeding with either PO or MM analysis of the transmission through the radome it is necessary to first compute the antenna field on the inner surface of the radome. This computation must be carried out with as much accuracy as possible since it will serve as the excitation field for the MM or hybrid PO-MM solutions.

The near-zone electromagnetic field can calculated from the following two equations:

$$\vec{E}_p = -j\omega\vec{A} - j\frac{1}{\omega\mu\epsilon}\nabla(\nabla\cdot\vec{A}) - \frac{1}{\epsilon}\nabla\times\vec{F} \tag{1a}$$

$$\vec{H}_p = -j\omega\vec{F} - j\frac{1}{\omega\mu\epsilon}\nabla(\nabla\cdot\vec{F}) + \frac{1}{\mu}\nabla\times\vec{A} \tag{1b}$$

where

$$\vec{A} = \frac{\mu}{4\pi}\int\int_{S_a}\vec{J}(\vec{r'})\frac{exp(-jkR)}{R}ds' \tag{2a}$$

$$\vec{F} = \frac{\epsilon}{4\pi}\int\int_{S_a}\vec{M}(\vec{r'})\frac{exp(-jkR)}{R}ds' \tag{2b}$$

and $R = |\vec{r} - \vec{r'}|$. Here, $vecJ(\vec{r'})$ and $\vec{M}(\vec{r'})$ represent the radiation currents on the antenna aperture or simply some externally provided sources. For reflector or waveguide-type aperture antennas,

$$\vec{J}(\vec{r'}) = \hat{n'} \times \vec{H}_a(\vec{r'})$$

$$\vec{M}(\vec{r'}) = \vec{E}_a(\vec{r'}) \times \hat{n'}$$

where $\vec{E}_a(\vec{r'})$ and $\vec{H}_a(\vec{r'})$ are the aperture fields.

To evaluate the integrals, we must carry out all differentiations first. We have

$$\nabla \times \vec{F} = \frac{\epsilon}{4\pi} \int\int_{S_a} \nabla \frac{\exp(-jkR)}{R} \times \vec{M}(\vec{r'})\, ds'$$

$$\nabla(\nabla \cdot \vec{F}) = \frac{\mu}{4\pi} \int\int_{S_a} \vec{J}(\vec{r'}) \cdot \nabla\nabla \frac{\exp(-jkR)}{R}\, ds'$$

and

$$\nabla \frac{\exp(-jk|\vec{r} - \vec{r'}|)}{|\vec{r} - \vec{r'}|} = -\frac{(1 + jkR)\exp(-jkR)}{R^3}\vec{R}$$

$$\nabla\nabla \frac{\exp(-jk|\vec{r} - \vec{r'}|)}{|\vec{r} - \vec{r'}|} = -\bar{\bar{I}}\frac{(1 + jkR)\exp(-jkR)}{R^3} + \frac{(3 - k^2R^2 + j3kR)\exp(-jkR)}{R^5}\vec{R}\vec{R}$$

$$\vec{R} = [(x - x')\hat{x} + (y - y')\hat{y} + (z - z')\hat{z}].$$

Substituting these into (1) gives

$$\vec{E}_p = \frac{-j\omega\mu}{4\pi} \int\int_{S_a} \left(\vec{J}(\vec{r'}) \frac{k^2R^2 - 1 - jkR}{k^2R^3} + [\vec{J}(\vec{r'}) \cdot \vec{R}]\vec{R} \frac{(3 - k^2R^2 + j3kR)}{k^2R^5} \right) \exp(-jkR) ds'$$

$$+ \int\int_{S_a} \frac{(1 + jkR)}{4\pi R^3} [\vec{R} \times \vec{M}(\vec{r'})] \exp(-jkR) ds' \qquad (3)$$

where

$$\vec{J}(\vec{r'}) = \hat{z} \times \vec{H}_a(\vec{r'}) = -H_{ay}(x', y')\hat{x} + H_{ax}(x', y')\hat{y}$$

$$\vec{M}(\vec{r'}) = \vec{E}_a(\vec{r'}) \times \hat{z} = E_{ay}(x', y')\hat{x} - E_{ax}(x', y')\hat{y}$$

If the "far-zone" relation

$$\vec{H}_a = \frac{1}{\eta}\hat{z} \times \vec{E}_a \qquad (4)$$

is further employed on the aperture, we get

$$\vec{J}(\vec{r'}) = -\frac{1}{\eta}E_{ax}(x', y')\hat{x} - \frac{1}{\eta}E_{ay}(x', y')\hat{y} = -\frac{1}{\eta}\vec{E}_a(\vec{r'}) \qquad (4')$$

and thus

$$\vec{E_p} = \frac{jk}{4\pi}\int\int_{S_a}\left(\vec{E_a}(\vec{r'})\frac{k^2R^2-1-jkR}{k^2R^3} + [\vec{E_a}(\vec{r'})\cdot\vec{R}]\vec{R}\frac{(3-k^2R^2+j3kR)}{k^2R^5}\right)\exp(-jkR)ds'$$

$$+\frac{jk}{4\pi}\int\int_{S_a}\frac{(1+jkR)}{jkR^3}[\vec{R}\times\vec{E_a}(\vec{r'})\times\hat{z}]\exp(-jkR)ds'$$

We can rewrite this in terms of spherical components by using transformations

$$\hat{x} = \sin\theta\cos\phi\hat{r} + \cos\theta\cos\phi\hat{\theta} - \sin\phi\hat{\phi}$$

$$\hat{y} = \sin\theta\sin\phi\hat{r} + \cos\theta\sin\phi\hat{\theta} + \cos\phi\hat{\phi}$$

$$\hat{z} = \cos\theta\hat{r} - \sin\theta\hat{\theta},$$

to get

$$E_\theta(x,y,z) = \int\int_{S_a} Q_\theta(x,y,z,x',y',z')\frac{\exp(-jkR)}{R}ds' \tag{5a}$$

$$E_\phi(x,y,z) = \int\int_{S_a} Q_\phi(x,y,z,x',y',z')\frac{\exp(-jkR)}{R}ds' \tag{5b}$$

where

$$Q_\theta(x,y,z,x',y',z') = [E_{ax}(\vec{r'})\cos\phi + E_{ay}(\vec{r'})\sin\phi]\cos\theta\left[\frac{k^2R^2-1-jkR}{k^2R^2}\right]$$

$$+[(x-x')E_{ax}(\vec{r'}) + (y-y')E_{ay}(\vec{r'})][(x-x')\cos\theta\cos\phi + (y-y')\cos\theta\sin\phi - (z-z')\sin\theta]$$
$$\frac{(3-k^2R^2+j3kR)}{k^2R^4}$$

$$+\left([E_{ax}(\vec{r'})\cos\phi + E_{ay}(\vec{r'})\sin\phi](z-z')\cos\theta + [(x-x')E_{ax}(\vec{r'}) + (y-y')E_{ay}(\vec{r'})]\sin\theta\right)\frac{(1+jkR)}{jkR^2}$$

$$Q_\phi(x,y,z,x',y',z') = [-E_{ax}(\vec{r'})\sin\phi + E_{ay}(\vec{r'})\cos\phi]\left[\frac{k^2R^2-1-jkR}{k^2R^2}\right]$$

$$+[(x-x')E_{ax}(\vec{r'}) + (y-y')E_{ay}(\vec{r'})][-(x-x')\sin\phi + (y-y')\cos\phi]\frac{(3-k^2R^2+j3kR)}{k^2R^4}$$

$$+[-E_{ax}(\vec{r'})\sin\phi + E_{ay}(\vec{r'})\cos\phi](z-z')\frac{(1+jkR)}{jkR^2}$$

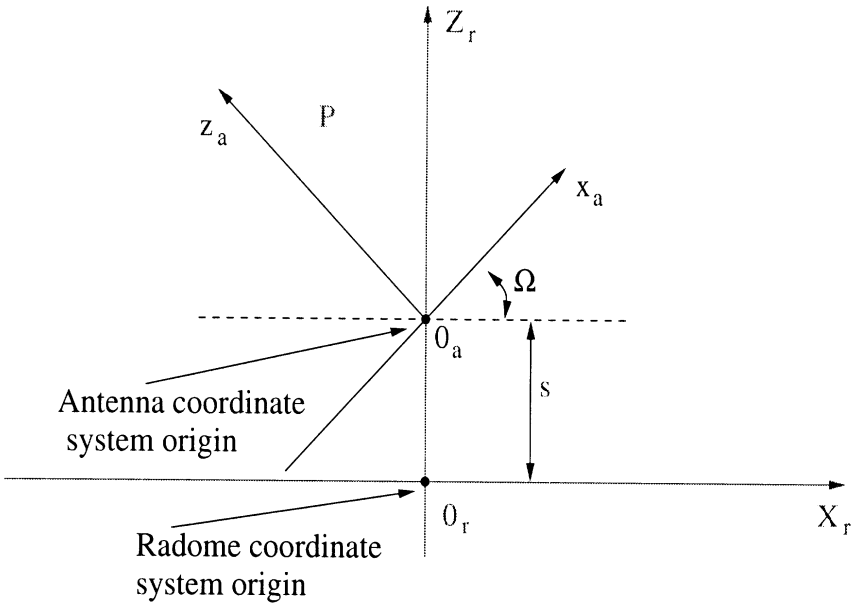

Figure 3: Coordinate transformation

2.2 Coordinate Transformation

One last step is the transformation from the antenna coordinate system $(x_a,\ y_a,\ z_a)$ to the radome system $(X_r,\ Y_r,\ Z_r)$. After having computed all the field components, we need consider the coordinate transformation as, shown in Figure 3.

Referring to Figure 3, the appropriate transformation is

$$\begin{bmatrix} X_r \\ Y_r \\ Z_r \end{bmatrix} = \begin{bmatrix} \cos\Omega & 0 & -\sin\Omega \\ 0 & 1 & 0 \\ \sin\Omega & 0 & \cos\Omega \end{bmatrix} \begin{bmatrix} x_a \\ y_a \\ z_a \end{bmatrix} + \begin{bmatrix} 0 \\ 0 \\ s \end{bmatrix} \tag{6a}$$

where s is shift distance between the two coordinate systems alone the radome axis. Alternatively, the inverse transformation is

$$\begin{bmatrix} x_a \\ y_a \\ z_a \end{bmatrix} = \begin{bmatrix} \cos\Omega & 0 & \sin\Omega \\ 0 & 1 & 0 \\ -\sin\Omega & 0 & \cos\Omega \end{bmatrix} \begin{bmatrix} X_r \\ Y_r \\ Z_r - s \end{bmatrix} \tag{6b}$$

Also, note that

$$r_a = \sqrt{x_a^2 + y_a^2 + z_a^2} = \sqrt{X_r^2 + Y_r^2 + (Z_r - s)^2} \tag{7a}$$

$$\phi_a = \tan^{-1}\frac{y_a}{x_a} = \tan^{-1}\frac{Y_r}{X_r\cos\Omega + (Z_r - s)\sin\Omega} \tag{7b}$$

$$\theta_a = \tan^{-1}\frac{\sqrt{x_a^2 + y_a^2}}{z_a} = \tan^{-1}\frac{\sqrt{[X_r\cos\Omega + (Z_r - s)\sin\Omega]^2 + Y_r^2}}{-X_r\sin\Omega + (Z_r - s)\cos\Omega} \tag{7c}$$

Because of the rotation angle Ω shown in Figure 3, the vector field components will be different after the transformation. Specifically, the θ and ϕ unit vectors in the two different coordinate systems will change as follows:

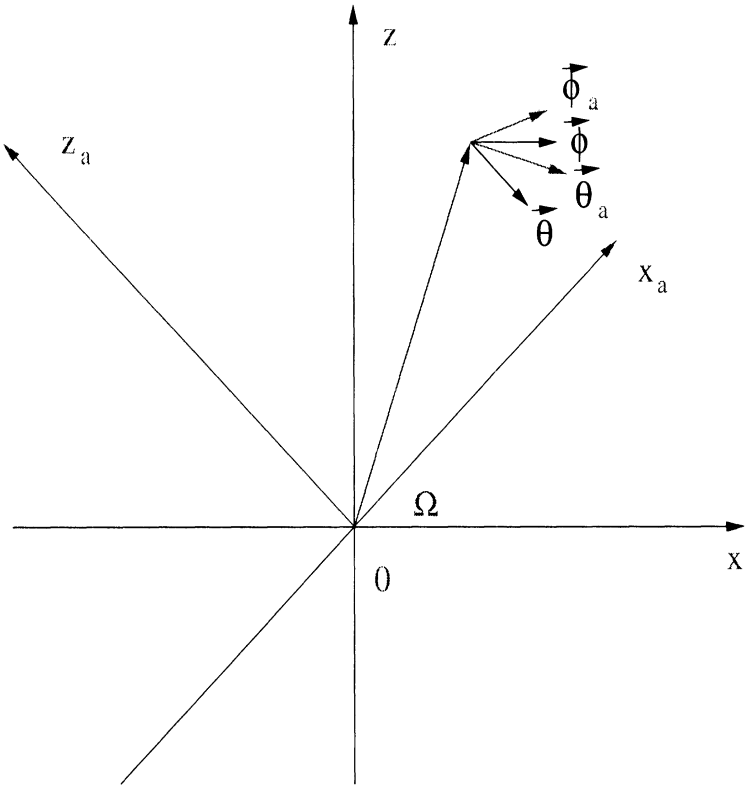

Figure 4: Unit vectors in two coordinate systems

$$\hat{\theta}_a = \alpha_{11}\hat{\theta} + \alpha_{12}\hat{\phi} \tag{8a}$$

$$\hat{\phi}_a = \alpha_{21}\hat{\theta} + \alpha_{22}\hat{\phi} \tag{8b}$$

where

$$\alpha_{11} = \alpha_{22} = \frac{(x^2 + y^2)\cos\Omega + xz\sin\Omega}{\sqrt{[(x\cos\Omega + z\sin\Omega)^2 + y^2](x^2 + y^2)}}$$

$$\alpha_{12} = \alpha_{21} = y\sin\Omega\sqrt{\frac{x^2 + y^2 + z^2}{[(x\cos\Omega + z\sin\Omega)^2 + y^2](x^2 + y^2)}}$$

2.3 Modal Decomposition of the Incident Fields

Having evaluated all field components in the radome coordinate system, we next proceed to decompose the antenna aperture field into cylindrical modes. Based on the well-known body of revolution (BOR), this decomposition is essential to taking advantage of the radome's geometry. Since the cylindrical mode has the same ρ-dependence for each ϕ-angle and the same is true with the geometry, the resulting scattered/transmitted field will have the same as the incident mode. Thus, it suffices to only evaluate the currents/fields on a single cross-section of the radome. Therefore, modal decomposition reduces the 3D problem to an equivalent 2D problem. However, each mode must now be analyzed separately and resulting currents/fields need to be summed to compute the total field transmitted through the radome.

At point P on radome's inside surface, the electric field components are given We begin by considering the original expression

$$\vec{E}_p = E_{pr}(z,\phi)\hat{r} + E_{p\theta}(z,\phi)\hat{\theta} + E_{p\phi}(z,\phi)\hat{\phi} \tag{9}$$

at point P on the radome. By invoking mode orthogonality, each of these components is expanded as follows:

$$E_{pr}(z,\phi) = \sum_{n=-N}^{N} \tilde{E}_{pr,n}(z)\exp(jn\phi) \tag{10a}$$

$$E_{p\theta}(z,\phi) = \sum_{n=-N}^{N} \tilde{E}_{p\theta,n}(z)\exp(jn\phi) \tag{10b}$$

$$E_{p\phi}(z,\phi) = \sum_{n=-N}^{N} \tilde{E}_{p\phi,n}(z)\exp(jn\phi) \tag{10c}$$

where

$$\tilde{E}_{pr,n}(z) = \frac{1}{2\pi}\int_0^{2\pi} E_{pr}(z,\phi)\exp(-jn\phi)d\phi$$

$$\tilde{E}_{p\theta,n}(z) = \frac{1}{2\pi}\int_0^{2\pi} E_{p\theta}(z,\phi)\exp(-jn\phi)d\phi$$

$$\tilde{E}_{p\phi,n}(z) = \frac{1}{2\pi}\int_0^{2\pi} E_{p\phi}(z,\phi)\exp(-jn\phi)d\phi.$$

A similar decomposition can be carried out for the magnetic field components. The final expressions are the same as those with the replacement E_s by H_s.

3 PO Approximation

This section describes the physical optics approximation for computing the field transmitted through radome. A key assumption in this approximation is that the radome is locally planar. The transmitted/reflected fields can then be computed using the place wave reflection/transmission coefficients for the thick dielectric slab. Based on the approximations for the reflected and transmitted fields, the equivalent electric and magnetic surface currents can then be obtained from

$$\vec{J}^{PO}(\vec{r'}) = \hat{n'} \times \vec{H}^{PO}(\vec{r'}) \tag{11a}$$

$$\vec{M}^{PO}(\vec{r'}) = \vec{E}^{PO}(\vec{r'}) \times \hat{n'}. \tag{11b}$$

As illustrated in Figs. 5 and 6, the two incident wave polarizations must be computed separately. The reflection coefficients for the perpendicular and parallel polarizations are are

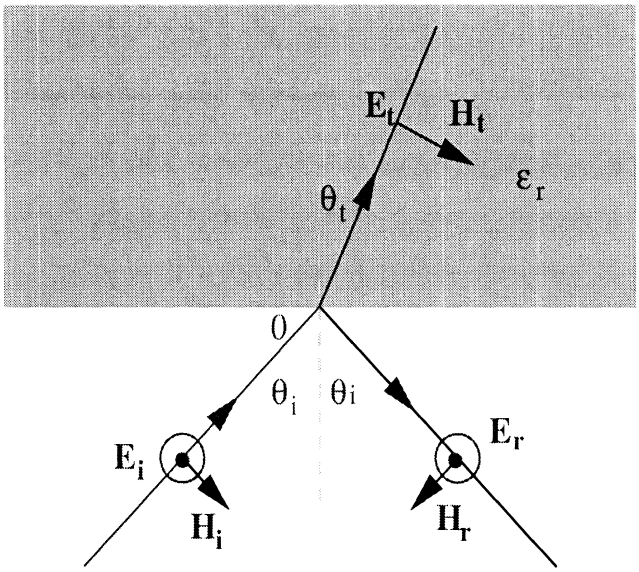

Figure 5: Reflection and transmission at a dielectric interface: perpendicular polarization.

$$R_1^{\perp} = \frac{\cos\theta_i - \sqrt{\epsilon_r - \sin^2(\theta_i)}}{\cos\theta_i + \sqrt{\epsilon_r - \sin^2(\theta_i)}} \tag{12a}$$

$$R_1^{//} = \frac{\epsilon_r \cos\theta_i - \sqrt{\epsilon_r - \sin^2(\theta_i)}}{\epsilon_r \cos\theta_i + \sqrt{\epsilon_r - \sin^2(\theta_i)}} \tag{12b}$$

and these refer to a simple dielectric interface.

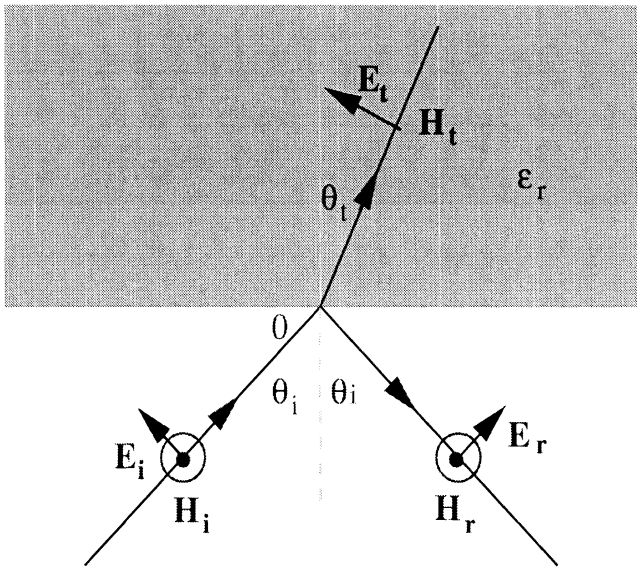

Figure 6: Reflection and transmission at a dielectric interface: parallel polarization.

For a finite thickness dielectric layer (as shown in Fig.7), we must consider multiple interactions. These can be accomplished for by the composite reflection and transmission coefficients,

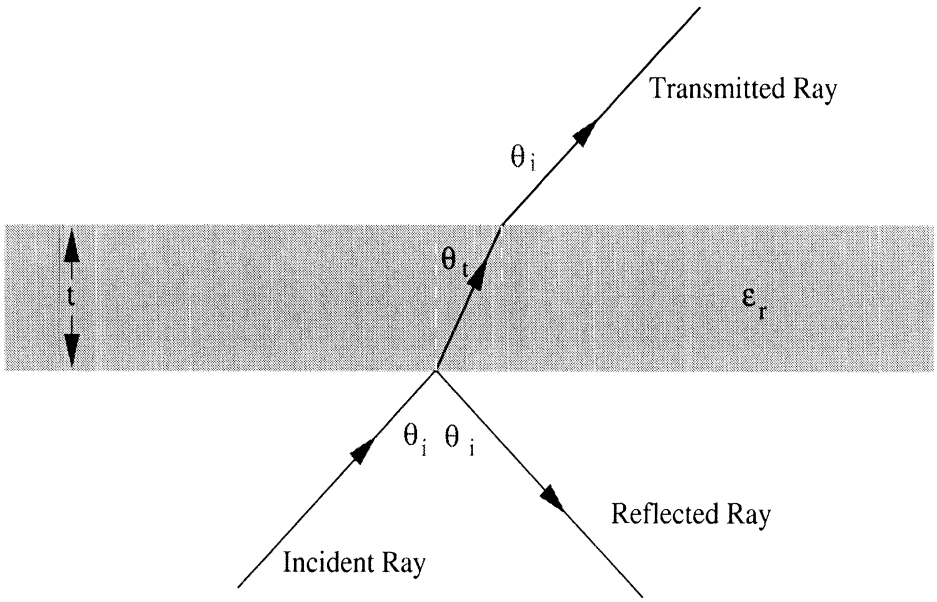

Figure 7: Reflection and transmission through a dielectric slab.

$$\Gamma = \frac{R_1(1 - P_d^2 P_a)}{1 - R_1^2 P_d^2 P_a} \tag{13a}$$

$$T = \frac{(1 - R_1^2) P_d}{1 - R_1^2 P_d^2 P_a} \tag{13b}$$

where

$$P_d = \exp\left(\frac{-jk_0\epsilon_r t}{\sqrt{\epsilon_r - \sin^2(\theta_i)}}\right)$$

$$P_a = \exp\left(\frac{j2k_0 t \sin^2(\theta_i)}{\sqrt{\epsilon_r - \sin^2(\theta_i)}}\right)$$

refer to the propagation delays through the layer of thickness t.

Contributions from multi-bounces within the radome can be evaluated using ray-tracing. Referring to Fig. 8, let us consider the incident ray direction

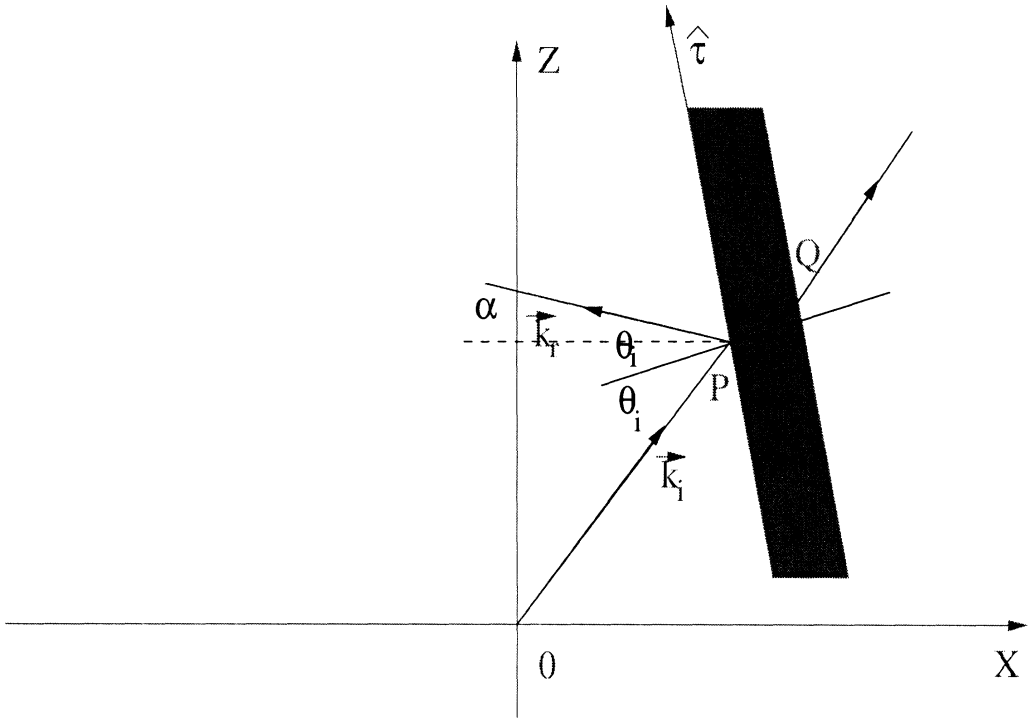

Figure 8: First-order PO solution

$$\hat{k}_i = \frac{x_p\hat{x} + y_p\hat{y} + z_p\hat{z}}{\sqrt{x_p^2 + y_p^2 + z_p^2}} \tag{14}$$

where

$$x_p = \rho_p \cos(\phi_p), \qquad y_p = \rho_p \sin(\phi_p), \qquad \rho_p = \rho(z_p).$$

To obtain the reflection angle, we note that the tangential and normal unit vectors at P are given by

$$\hat{\tau}_p = \frac{\rho_i'(z_p)(\hat{x}\cos\phi_p + \hat{y}\sin\phi_p) + \hat{z}}{\sqrt{[\rho_i'(z_p)]^2 + 1}} \tag{15a}$$

and

$$\hat{n_p} = \frac{\hat{x}\cos\phi_p + \hat{y}\sin\phi_p - \rho_i'(z_p)\hat{z}}{\sqrt{[\rho_i'(z_p)]^2 + 1}}. \tag{15b}$$

Thus, Snell's reflection angle is given by

$$\theta_i = \cos^{-1}(\hat{k}_i \cdot \hat{n_p}) \tag{16}$$

and the z distance between the entry and exit point of the layer is found from

$$\delta_z = z_q - z_p = t_p \left[\frac{\sin\theta_i}{\sqrt{\epsilon_r - \sin^2\theta_i}} \frac{1}{\sqrt{[\rho_i'(z_p)]^2 + 1}} + \frac{\rho_i'(z_p)}{\sqrt{[\rho_i'(z_p)]^2 + 1}} \right] \tag{17}$$

Also, the angle α of the reflected ray with respect to the horizontal is given

$$\alpha_p = 2\theta_i + \theta_p - \frac{\pi}{2} \tag{18}$$

where

$$t_p = \frac{\rho_e(z_p) - \rho_i(z_p)}{\sqrt{[\rho_i'(z_p)]^2 + 1}}, \qquad \theta_p = tan^{-1}(\frac{\rho_p}{z_p})$$

The following table summarizes the incident, reflected, and transmitted ray fields at an arbitrary point P on the interior surface of the radome. In the table, $E_{p\theta}(\theta_a, \phi_a)$ and $E_{p\phi}(\theta_a, \phi_a)$

Ray	Perpendicular polarization	Parallel polarization
Incident ray	$E_{\perp}^{i} = E_{p\phi}(\theta_a, \phi_a)$	$E_{//}^{i} = E_{p\theta}(\theta_a, \phi_a)$
Reflected ray	$E_{\perp}^{r} = \Gamma_{\perp} E_{p\phi}(\theta_a, \phi_a)$	$E_{//}^{r} = \Gamma_{//} E_{p\theta}(\theta_a, \phi_a)$
Transmitted ray	$E_{\perp}^{t} = T_{\perp} E_{p\phi}(\theta_a, \phi_a)$	$E_{//}^{t} = T_{//} E_{p\theta}(\theta_a, \phi_a)$

are given in (9) and (10). The PO currents $\vec{J}_{1,2}^{PO}$ and $\vec{M}_{1,2}^{PO}$ are evaluated as

$$\vec{J}_1^{PO} = \hat{n}_1 \times (\vec{H}^i + \vec{H}^r) \tag{19a}$$

$$\vec{M}_1^{PO} = \vec{E}^i + \vec{E}^r) \times \hat{n}_1 \tag{19b}$$

$$\vec{J}_2^{PO} = \hat{n}_2 \times \vec{H}^t \tag{20a}$$

$$\vec{M}_2^{PO} = \vec{E}^t \times \hat{n}_2 \tag{20b}$$

where $\hat{n}_1$ and $\hat{n}_2$ are illustrated in the following figure.

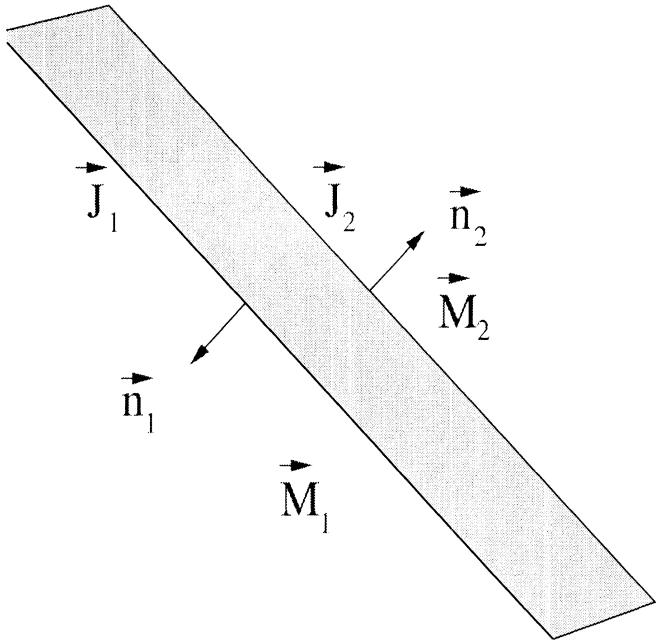

4 Integral Equation Formulation

This section develops the combined field integral equation formulation for evaluating the radiation from an antenna enclosed in a dielectric radome. Figure 9 shows the geometry of the problem being considered. In proceeding to the formulation, we identify regions 1, 2, 3, and boundary surfaces S_1 and S_2, as shown in Figure 9. The dielectric radome is denoted as Region 2 and the exterior free space is denoted as Region 3. The antenna is in Region 1 (interior of the radome) and is illuminating the boundary surface S_1, i.e. the interior surface of the radome. The equivalent electric and magnetic surface currents on the interior surface of the radome will be denoted as J_1 and M_1. Similarly, the equivalent electric and magnetic surface currents over the outside surface of the radome will be denoted as J_2 and M_2.

4.1 Surface Integral Equations

Based on the usual moment method procedure for multi layer dielectrics [1-8] for axisymmetric structures, we begin by introducing equivalent currents on each cross-sectional boundary separating the three regions of interest. Using these equivalent currents, the field in each region can be expressed as follows.

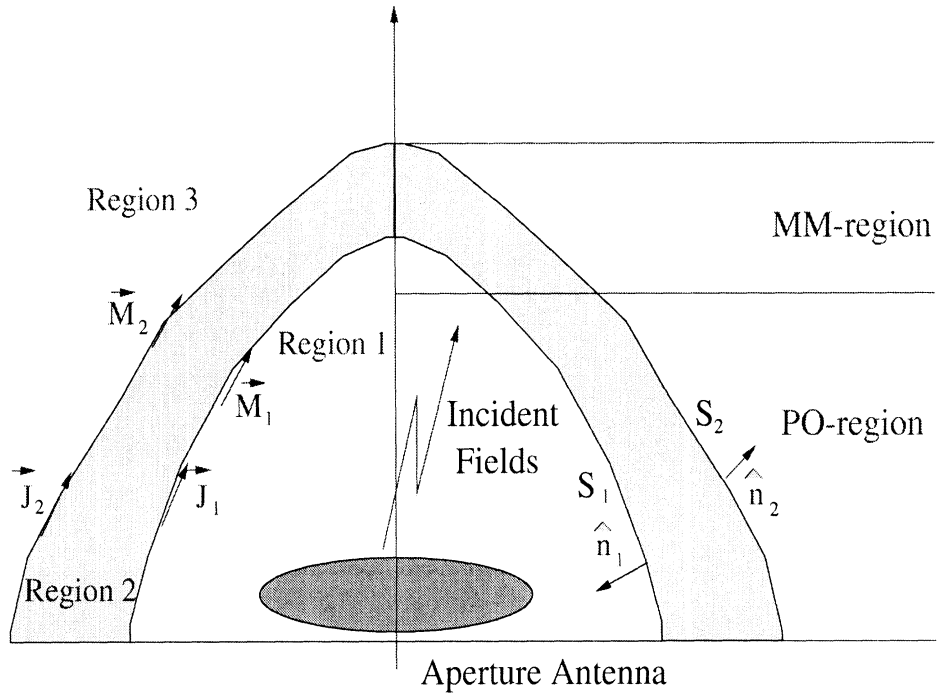

Figure 9: Geometry of the problem considered.

Region 1 (interior of radome):

$$\theta(\vec{r})\vec{E}_1 = \vec{E}^{inc} - \mathbf{L}_1\vec{J}_1(\vec{r}') + \mathbf{K}_1\vec{M}_1(\vec{r}') \tag{21a}$$

$$\theta(\vec{r})\vec{H}_1 = \vec{H}^{inc} - \mathbf{K}_1\vec{J}_1(\vec{r}') - \frac{1}{\eta_1^1}\mathbf{L}_2\vec{M}_2(\vec{r}') \tag{21b}$$

where $\theta(\vec{r})$ is the Heaviside function and is defined as

$$\theta(\vec{r}) = \begin{bmatrix} 1; for \ \ \vec{r} \in R_2 \\ 1/2; for \ \ \vec{r} \in S \\ 0; otherwise. \end{bmatrix} \tag{22}$$

Here, the electric and magnetic surface currents $\vec{J}_1$ and $\vec{M}_1$ are related to fields on

$$\vec{J}_1 = \hat{n}_1 \times \vec{H}_1|_S, \quad \vec{M}_1 = \vec{E}_1|_S \times \hat{n}_1$$

and introduced on the interior surface of the radome. The integro-differential operator L_i and K_i $(i = 1, 2, 3)$ are defined as [1]

$$\mathbf{L}_i\vec{X}(\vec{r}) = j\omega\mu_i \int_S \left[\vec{X}(\vec{r}') + \frac{1}{k_i^2}\nabla\nabla' \cdot \vec{X}(\vec{r}')\right] G(k_i|\vec{r} - \vec{r}'|)ds' \tag{23a}$$

and

$$\mathbf{K}_i\vec{X}(\vec{r}) = \int_S \vec{X}(\vec{r'}) \times \nabla G(k_i|\vec{r} - \vec{r'}|)ds' \tag{23b}$$

where the Green's function is given by

$$G(k_i|\vec{r} - \vec{r'}|) = \frac{\exp(-jk_i|\vec{r} - \vec{r'}|)}{4\pi|\vec{r} - \vec{r'}|}. \tag{24}$$

and $k_i^2 = \omega^2\mu_i\epsilon_i$. Similarly, for the other regions, the fields are given by

Region 2:

$$\theta(\vec{r})\vec{E}_2 = \mathbf{L}_2\vec{J}_1(\vec{r'}) - \mathbf{K}_2\vec{M}_1(\vec{r'}) + \mathbf{L}_2\vec{J}_2(\vec{r'}) - \mathbf{K}_2\vec{M}_2(\vec{r'}) \tag{25a}$$

$$\theta(\vec{r})\vec{H}_2 = \mathbf{K}_2\vec{J}_1(\vec{r'}) + \frac{1}{\eta_2^2}\mathbf{L}_2\vec{M}_1(\vec{r'}) + \mathbf{K}_2\vec{J}_2(\vec{r'}) + \frac{1}{\eta_2^2}\mathbf{L}_2\vec{M}_2(\vec{r'}) \tag{25b}$$

Region 3:

$$\theta(\vec{r})\vec{E}_3 = -\mathbf{L}_3\vec{J}_2(\vec{r'}) + \mathbf{K}_3\vec{M}_2(\vec{r'}) \tag{26a}$$

$$\theta(\vec{r})\vec{H}_3 = -\mathbf{K}_3\vec{J}_2(\vec{r'}) - \frac{1}{\eta_3^2}\mathbf{L}_3\vec{M}_2(\vec{r}) \tag{26b}$$

where the electric and magnetic surface currents $\vec{J}_2$ and $\vec{M}_2$ are

$$\vec{J}_2 = \hat{n}_2 \times \vec{H}_3|_S, \quad \vec{M}_2 = \vec{E}_3|_S \times \hat{n}_2$$

and reside on the exterior radome surface.

Employing the above equations and enforcing the boundary conditions of the total tangential electric and magnetic field continuity across the surface, we obtain the combined field integral equations:

$$(\mathbf{L}_1 + \mathbf{L}_2)\vec{J}_1(\vec{r'}) - (\mathbf{K}_1 + \mathbf{K}_2)\vec{M}_1(\vec{r'}) + \mathbf{L}_2\vec{J}_2(\vec{r'}) - \mathbf{K}_2\vec{M}_2(\vec{r'}) = \vec{E}^{inc}, \quad on\ S_1 \tag{27a}$$

$$(\mathbf{K}_1 + \mathbf{K}_2)\vec{J}_1(\vec{r'}) + (\frac{1}{\eta_1^2}\mathbf{L}_1 + \frac{1}{\eta_2^2}\mathbf{L}_2)\vec{M}_1(\vec{r'}) + \mathbf{K}_2\vec{J}_2(\vec{r'}) + \frac{1}{\eta_2^2}\mathbf{L}_2\vec{M}_2(\vec{r'}) = \vec{H}^{inc}, \quad on\ S_1 \tag{27b}$$

$$\mathbf{L}_2\vec{J}_1(\vec{r'}) - \mathbf{K}_2\vec{M}_1(\vec{r'}) + (\mathbf{L}_2 + \mathbf{L}_3)\vec{J}_2(\vec{r'}) - (\mathbf{K}_2 + \mathbf{K}_3)\vec{M}_2(\vec{r'}) = 0, \quad on\ S_2 \tag{27c}$$

$$\mathbf{K}_2\vec{J}_1(\vec{r'}) + \frac{1}{\eta_2^2}\mathbf{L}_2\vec{M}_1(\vec{r'}) + (\mathbf{K}_2 + \mathbf{K}_3)\vec{J}_2(\vec{r'}) + (\frac{1}{\eta_2^2}\mathbf{L}_2 + \frac{1}{\eta_3^2}\mathbf{L}_3)\vec{M}_2(\vec{r'}) = 0, \quad on\ S_2. \tag{27d}$$

where $\vec{E}^{inc}$ and $\vec{H}^{inc}$ are the incident fields from the aperture antenna, as given in (9).

4.2 Moment Method Solution

The integral equations (27a)-(27d) can be solved by the method of moments for the surface equivalent electric and magnetic currents $\vec{J}_1$, $\vec{M}_1$, $\vec{J}_2$, and $\vec{M}_2$. To do so, we proceed to discretize the unknown electric and magnetic currents into a finite series of basis functions spanning the surfaces S_1 and S_2 as follows:

$$\vec{J}_1(\vec{r}) = \sum_{n,k} (a^t_{1,nk}\vec{J}^t_{nk} - a^\phi_{1,nk}\vec{J}^\phi_{nk}) \tag{28a}$$

$$\vec{M}_1(\vec{r}) = \eta_0 \sum_{n,k} (b^t_{1,nk}\vec{J}^t_{nk} - b^\phi_{1,nk}\vec{J}^\phi_{nk}) \tag{28b}$$

$$\vec{J}_2(\vec{r}) = \sum_{n,k} (a^t_{2,nk}\vec{J}^t_{nk} - a^\phi_{2,nk}\vec{J}^\phi_{nk}) \tag{28c}$$

$$\vec{M}_2(\vec{r}) = \eta_0 \sum_{n,k} (b^t_{2,nk}\vec{J}^t_{nk} - b^\phi_{2,nk}\vec{J}^\phi_{nk}) \tag{28d}$$

where

$$\vec{J}^\alpha_{nk} = \hat{u}_\alpha \frac{T_k}{\rho(t)} \exp(jn\phi)$$

and T_k is the triangle function spanning the k-th annulus with four segments, as shown in Fig. 10.

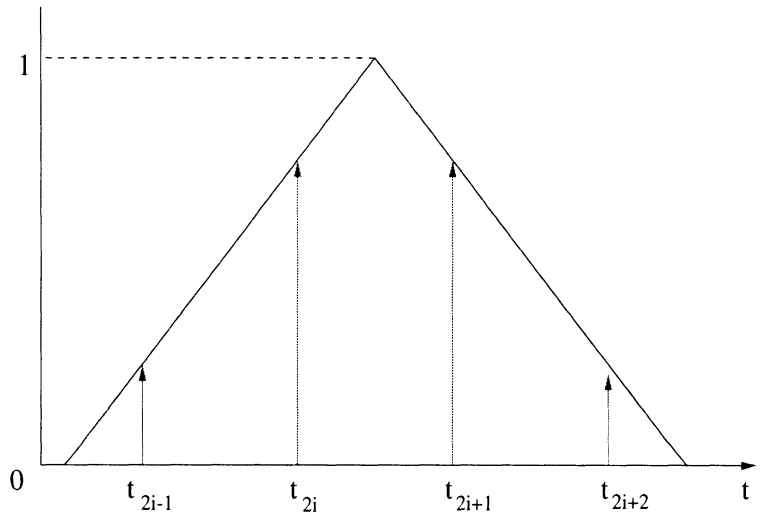

Figure 10: Triangle function and four impulse approximation.

Substituting the above basis functions and using Galerkin method (testing function $\vec{W}_{nk}^{\alpha} = \vec{J}_{nk}^{\alpha}$), we can derive the following matrix equation.

$$\begin{bmatrix} \mathbf{L}_1+\mathbf{L}_2 & -(\mathbf{K}_1+\mathbf{K}_2) & \mathbf{L}_2 & -\mathbf{K}_2 \\ \mathbf{K}_1+\mathbf{K}_2 & \frac{\mathbf{L}_1}{\eta_1^2}+\frac{\mathbf{L}_2}{\eta_2^2} & \mathbf{K}_2 & \frac{\mathbf{L}_2}{\eta_2^2} \\ \mathbf{L}_2 & -\mathbf{K}_2 & (\mathbf{L}_2+\mathbf{L}_3) & -(\mathbf{K}_2+\mathbf{K}_3) \\ \mathbf{K}_2 & \frac{\mathbf{L}_2}{\eta_2^2} & \mathbf{K}_2+\mathbf{K}_3 & \frac{\mathbf{L}_2}{\eta_2^2}+\frac{\mathbf{L}_3}{\eta_3^2} \end{bmatrix} \begin{bmatrix} \mathbf{a}_1 \\ \mathbf{b}_1 \\ \mathbf{a}_2 \\ \mathbf{b}_2 \end{bmatrix} = \begin{bmatrix} \tilde{\mathbf{E}}^{inc} \\ \tilde{\mathbf{H}}^{inc} \\ 0 \\ 0 \end{bmatrix} \tag{29}$$

The $\mathbf{L}$ operator has the form of

$$\begin{bmatrix} \mathbf{L}^{tt} & \mathbf{L}^{t\phi} \\ \mathbf{L}^{\phi t} & \mathbf{L}^{\phi\phi} \end{bmatrix} \tag{30}$$

where

$$L_{kl}^{tt} = \sum_{p,q=1}^{4} \left[j\omega\mu T_p T_q (\sin v_p \sin v_q G_{cn} + \cos v_p \cos v_q G_n) - \frac{j}{\omega\epsilon} \bar{T}_p \bar{T}_q G_n \right] \tag{31a}$$

$$L_{kl}^{\phi t} = -\sum_{p,q=1}^{4} \left[\omega\mu T_p T_q \sin v_q G_{sn} + \frac{n}{\omega\epsilon\rho_p} \bar{T}_p \bar{T}_q G_n \right] \tag{31b}$$

$$L_{kl}^{t\phi} = -\sum_{p,q=1}^{4} \left[\omega\mu T_p T_q \sin v_p G_{sn} + \frac{n}{\omega\epsilon\rho_p} \bar{T}_q \bar{T}_q G_n \right] \tag{31c}$$

$$L_{kl}^{\phi\phi} = -\sum_{p,q=1}^{4} T_p T_q \left[j\omega\mu G_{cn} + \frac{n^2}{j\omega\epsilon\rho_p\rho_q} G_n \right] \tag{31d}$$

with

$$G_n = \Delta t_p \Delta t_q \int_0^{\pi} g(\phi) \cos(n\phi) d\phi$$

$$G_{cn} = \Delta t_p \Delta t_q \int_0^{\pi} g(\phi) \cos(n\phi) \cos\phi d\phi$$

$$G_n = \Delta t_p \Delta t_q \int_0^{\pi} g(\phi) \cos(n\phi) \sin\phi d\phi$$

and

$$g(\phi) = \frac{\exp(-jkR_{pq})}{R_{pq}}$$

$$R_{pq} = \begin{bmatrix} \sqrt{(\rho_p-\rho_q)^2+(z_p-z_q)^2+2\rho_p\rho_q(1-\cos\phi)}, if\ p \neq q \\ \sqrt{(\Delta t_p/4)^2+2\rho_p^2(1-\cos\phi)}, if\ p = q \end{bmatrix}$$

The $\mathbf{K}$ operator has the form of

$$\begin{bmatrix} \mathbf{K}^{tt} & \mathbf{K}^{t\phi} \\ \mathbf{K}^{\phi t} & \mathbf{K}^{\phi\phi} \end{bmatrix} \tag{32}$$

where

$$K_{kl}^{tt} = -j\eta_0 \sum_{p,q=1}^{4} T_p T_q H_{sn} \left[\sin v_p \sin v_q (z_p - z_q) + \rho_q \sin v_p \cos v_q - \rho_p \cos v_q \sin v_q\right] \tag{33a}$$

$$K_{kl}^{\phi t} = \eta_0 \sum_{p,q=1}^{4} T_p T_q \left[(\sin v_q (z_p - z_q) + \rho_q \cos v_q) H_{cn} - \rho_p \cos v_q H_n\right] \tag{33b}$$

$$K_{kl}^{t\phi} = -\eta_0 \sum_{p,q=1}^{4} T_p T_q \left[(-\sin v_p (z_p - z_q) + \rho_p \cos v_p) H_{cn} - \rho_q \cos v_p H_n\right] \tag{33c}$$

$$K_{kl}^{\phi\phi} = j\eta_0 \sum_{p,q=1}^{4} (z_p - z_q) T_p T_q H_{sn} \tag{33d}$$

with

$$H_n = \Delta t_p \Delta t_q \int_0^{\pi} h(\phi) \cos(n\phi) d\phi$$

$$H_{cn} = \Delta t_p \Delta t_q \int_0^{\pi} h(\phi) \cos(n\phi) \cos\phi d\phi$$

$$H_n = \Delta t_p \Delta t_q \int_0^{\pi} h(\phi) \cos(n\phi) \sin\phi d\phi$$

and

$$h(\phi) = \frac{(1 + jkR_{pq}) \exp(-jkR_{pq})}{R_{pq}^3}.$$

The right-hand side of the matrix equation (29) can be written as follows.

$$\tilde{E}_{t,nk}^{inc} = 2\pi \int_{k-thsegment} T_k(t) \tilde{E}_{tn}^{inc} dt \tag{34a}$$

$$\tilde{E}_{\phi,nk}^{inc} = 2\pi \int_{k-thsegment} T_k(t) \tilde{E}_{\phi n}^{inc} dt \tag{34b}$$

$$\tilde{H}_{t,nk}^{inc} = 2\pi\eta_0 \int_{k-thsegment} T_k(t) \tilde{H}_{tn}^{inc} dt \tag{35a}$$

$$\tilde{H}_{\phi,nk}^{inc} = 2\pi\eta_0 \int_{k-thsegment} T_k(t) \tilde{H}_{\phi n}^{inc} dt. \tag{35b}$$

Solution of the matrix equation (29) gives the surface equivalent electric and magnetic currents on the radome surface. This moment method solution is accurate and suitable for relatively

small radomes. For electrically very large radomes (such as 100 wavelength long radome), the MM solution is a formidable task. In order to alleviate this difficulty, next subsection introduces a new hybrid PO-MM technique for the analysis of very radomes.

4.3 Hybrid PO-MM Solution

As shown in Fig. 9, the entire radome surface is divided into two parts: MM-region and PO-region. The moment method described in the previous subsection is applied to the MM-region, and the PO-region is modeled by the physical optics approximation introduced in Section 3. The corresponding equivalent surface currents are denoted by $\vec{J}_1^{MM}$, $\vec{M}_1^{MM}$, $\vec{J}_2^{MM}$, $\vec{M}_2^{MM}$ and $\vec{J}_1^{PO}$, $\vec{M}_1^{PO}$, $\vec{J}_2^{PO}$, $\vec{M}_2^{PO}$ for the MM-region and PO-region, respectively. Having invoked the PO approximation presented in Section 3, we obtain the PO currents $\vec{J}_1^{PO}$, $\vec{M}_1^{PO}$, $\vec{J}_2^{PO}$ and $\vec{M}_2^{PO}$. These known currents are then incorporated into the matrix equation (29) in the following manner.

$$\begin{bmatrix} \mathbf{L}_1^{MM}+\mathbf{L}_2^{MM} & -(\mathbf{K}_1^{MM}+\mathbf{K}_2^{MM}) & \mathbf{L}_2^{MM} & -\mathbf{K}_2^{MM} \\ \mathbf{K}_1^{MM}+\mathbf{K}_2^{MM} & \frac{\mathbf{L}_1^{MM}}{\eta_1^2}+\frac{\mathbf{L}_2^{MM}}{\eta_2^2} & \mathbf{K}_2^{MM} & \frac{\mathbf{L}_2^{MM}}{\eta_2^2} \\ \mathbf{L}_2^{MM} & -\mathbf{K}_2^{MM} & (\mathbf{L}_2^{MM}+\mathbf{L}_3^{MM}) & -(\mathbf{K}_2^{MM}+\mathbf{K}_3^{MM}) \\ \mathbf{K}_2^{MM} & \frac{\mathbf{L}_2^{MM}}{\eta_2^2} & \mathbf{K}_2^{MM}+\mathbf{K}_3^{MM} & \frac{\mathbf{L}_2^{MM}}{\eta_2^2}+\frac{\mathbf{L}_3^{MM}}{\eta_3^2} \end{bmatrix} \begin{bmatrix} \mathbf{a}_1^{MM} \\ \mathbf{b}_1^{MM} \\ \mathbf{a}_2^{MM} \\ \mathbf{b}_2^{MM} \end{bmatrix}$$

$$= \begin{bmatrix} \tilde{\mathbf{E}}^{inc}-(\mathbf{L}_1^{MP}+\mathbf{L}_2^{MP})\mathbf{a}_1^{PO}+(\mathbf{K}_1^{MP}+\mathbf{K}_2^{MP})\mathbf{b}_1^{PO}-\mathbf{L}_2^{MP}\mathbf{a}_2^{PO}+\mathbf{K}_2^{MP}\mathbf{b}_2^{PO} \\ \tilde{\mathbf{H}}^{inc}-(\mathbf{K}_1^{MP}+\mathbf{K}_2^{MP})\mathbf{a}_1^{PO}-(\frac{\mathbf{L}_1^{MP}}{\eta_1^2}+\frac{\mathbf{L}_2^{MP}}{\eta_2^2})\mathbf{b}_1^{PO}-\mathbf{K}_2^{MP}\mathbf{a}_2^{PO}-\frac{\mathbf{L}_2^{MP}}{\eta_2^2}\mathbf{b}_2^{PO} \\ -\mathbf{L}_2^{MP}\mathbf{a}_1^{PO}+\mathbf{K}_2^{MP}\mathbf{b}_1^{PO}-(\mathbf{L}_2^{MP}+\mathbf{L}_3^{MP})\mathbf{a}_2^{PO}+(\mathbf{K}_2^{MP}+\mathbf{K}_3^{MP})\mathbf{b}_2^{PO} \\ -\mathbf{K}_2^{MP}\mathbf{a}_1^{PO}-\frac{\mathbf{L}_2^{MP}}{\eta_2^2}\mathbf{b}_1^{PO}-(\mathbf{K}_2^{MP}+\mathbf{K}_3^{MP})\mathbf{a}_2^{PO}-(\frac{\mathbf{L}_2^{MP}}{\eta_2^2}+\frac{\mathbf{L}_3^{MP}}{\eta_3^2})\mathbf{b}_2^{PO} \end{bmatrix} \tag{36}$$

where the operators $\mathbf{L}_i^{Mk}$ and $\mathbf{K}_i^{Mk}$ ($i = 1, 2, 3$ for regions 1,2,3, respectively, and $j = M, P$ for MM-region and PO-region, respectively) are defined in (30) and (32) for different parts of the boundary and different associated regions. are coefficients $\mathbf{a}_1^{PO}$, $\mathbf{b}_1^{PO}$, $\mathbf{a}_2^{PO}$, and $\mathbf{b}_2^{PO}$ are related to PO currents $\vec{J}_1^{PO}$, $\vec{M}_1^{PO}$, $\vec{J}_2^{PO}$ and $\vec{M}_2^{PO}$ on

$$\mathbf{a}_1^{PO} = J_1^{PO}\rho_i \tag{37a}$$

$$\mathbf{b}_1^{PO} = M_1^{PO}\rho_i \tag{37b}$$

$$\mathbf{a}_2^{PO} = J_2^{PO}\rho_e \tag{37c}$$

$$\mathbf{b}_2^{PO} = M_2^{PO}\rho_e. \tag{37d}$$

Here ρ_i and ρ_e are the radii of points on the interior and exterior surface of the radome, respectively. Equation (36) is the hybrid PO-MM matrix equation and can be solved for the MM currents $J_1^{MM} = \frac{\mathbf{a}_1^{MM}}{\rho_i}$, $M_1^{MM} = \frac{\mathbf{b}_1^{MM}}{\rho_i}$, $J_2^{MM} = \frac{\mathbf{a}_2^{MM}}{\rho_e}$ and $M_2^{MM} = \frac{\mathbf{b}_2^{MM}}{\rho_e}$. Having MM currents $\vec{J}_2^{MM}$ and $\vec{M}_2^{MM}$ and using the PO currents $\vec{J}_2^{PO}$ and $\vec{M}_2^{PO}$ on the exterior surface of the radome, we can then proceed to compute the far-zone radiation pattern of the radome-enclosed antenna.

4.4 Far-Zone Radiation Pattern

Once $\vec{J}_2$ and $\vec{M}_2$ (from MM and PO) are found, the computation of the far zone field is obtained from the radiating integral following standard steps. For the far-region radiated field, we have

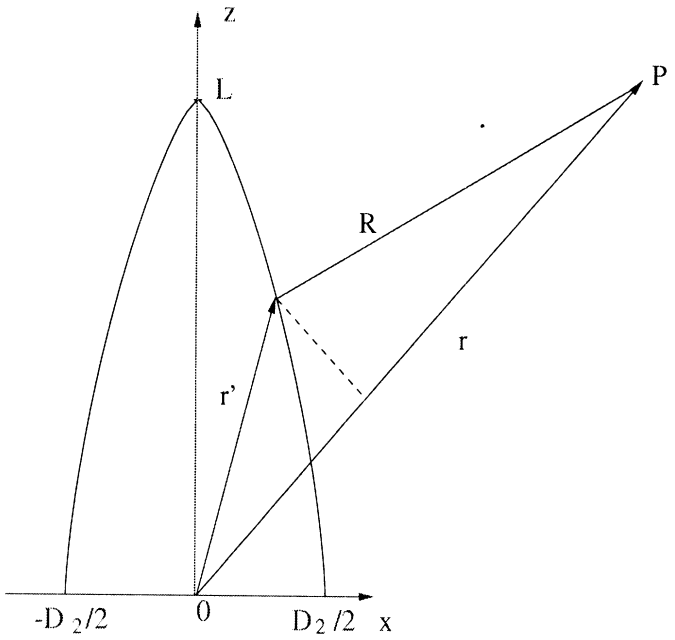

Figure 11: Calculation of far-region radiation pattern.

$$\vec{E} = \frac{-jk\exp(-jkr)}{4\pi r}\int_0^L\int_0^{2\pi}\left(\hat{n}\times[\hat{k}_s\times\vec{E}_s(\vec{r'})] + \hat{r}\times[\hat{n}\times\vec{E}_s(\vec{r'})]\right)\exp(jk_0\hat{r}\cdot\vec{r'})dS' \tag{38}$$

where $\eta\vec{H}_s = \hat{k}_s \times \vec{E}_s$ is understood. The θ and ϕ components can be decomposed from this to get

$$E_\theta = \frac{-jk\exp(-jkr)}{4\pi r}\int_0^L\int_0^{2\pi}\left(\hat{n}\times[\hat{k}_s\times\vec{E}_s(\vec{r'})]|_\theta - \hat{r}\times[\hat{n}\times\vec{E}_s(\vec{r'})]|_\phi\right)\exp(jk_0\hat{r}\cdot\vec{r'})dS' \quad (39a)$$

$$E_\phi = \frac{-jk\exp(-jkr)}{4\pi r}\int_0^L\int_0^{2\pi}\left(\hat{n}\times[\hat{k}_s\times\vec{E}_s(\vec{r'})]|_\phi + \hat{r}\times[\hat{n}\times\vec{E}_s(\vec{r'})]|_\theta\right)\exp(jk_0\hat{r}\cdot\vec{r'})dS' \quad (39b)$$

where the integrands can be explicitly expanded to give

$$\begin{aligned}&\hat{n}\times[\hat{k}_s\times\vec{E}_s(\vec{r'})]|_\theta - \hat{r}\times[\hat{n}\times\vec{E}_s(\vec{r'})]|_\phi\\ &= \frac{E_{s\theta}[\rho_e'(z_s')(\cos\theta+\cos\theta') - \sin\theta']\cos(\phi-\phi') - E_{s\theta}\sin\theta}{\sqrt{1+[\rho_e'(z_s')]^2}}\\ &+\frac{E_{s\phi}[\rho_e'(z_s') - \sin\theta'\cos\theta + \rho_e'(z_s')\cos\theta\cos\theta']\sin(\phi-\phi')}{\sqrt{1+[\rho_e'(z_s')]^2}}\end{aligned}$$

and

$$\begin{aligned}&\hat{n}\times[\hat{k}_s\times\vec{E}_s(\vec{r'})]|_\phi + \hat{r}\times[\hat{n}\times\vec{E}_s(\vec{r'})]|_\theta\\ &= \frac{E_{s\theta}[-\rho_e'(z_s') + \cos\theta\sin\theta' - \rho_e'(z_s')\cos\theta\cos\theta']\sin(\phi-\phi')}{\sqrt{1+[\rho_e'(z_s')]^2}}\\ &+\frac{E_{s\phi}[\rho_e'(z_s')(\cos\theta+\cos\theta') - \sin\theta']\cos(\phi-\phi') - E_{s\phi}\sin\theta}{\sqrt{1+[\rho_e'(z_s')]^2}}.\end{aligned}$$

The double integral in (39) can be reduced to a single integral by introducing the modal expansion

$$\vec{E}_s(\vec{r'}) = \vec{E}_s(z_s',\phi') = \sum_{n=-N}^{N}\tilde{\vec{E}}_s(z_s')\exp(jn\phi') \quad (40)$$

and the the identities

$$\hat{r}\cdot\vec{r'} = z_s\cos\theta + \rho_s\sin\theta\cos(\phi-\phi')$$

$$\int_0^{2\pi}\exp(jk\hat{r}\cdot\vec{r'})d\phi' = \exp(jkz_s\cos\theta + jn\phi)2\pi j^n J_n(k\rho_s\sin\theta)$$

$$\int_0^{2\pi}\exp(jk\hat{r}\cdot\vec{r'})\cos(\phi-\phi')d\phi' = \exp(jkz_s\cos\theta + jn\phi)2\pi j^{n-1}J_n'(k\rho_s\sin\theta)$$

$$\int_0^{2\pi}\exp(jk\hat{r}\cdot\vec{r'})\sin(\phi-\phi')d\phi' = -\exp(jkz_s\cos\theta + jn\phi)2n\pi j^n\frac{J_n(k\rho_s\sin\theta)}{k\rho_s\sin\theta}$$

The final expressions for the far-zone radiated E-field are then given by

$$E_\theta = \frac{-jk\exp(-jkr)}{2r}\sum_n\int_0^L\frac{j^{n-1}\rho_e(z_s')dz_s'}{\sqrt{1+[\rho_e'(z_s')]^2}}\left(\tilde{E}_{s\theta}I_{1n} + \tilde{E}_{s\theta}I_{2n} + \tilde{E}_{s\phi}I_{3n}\right)\exp(jkz_s\cos\theta + jn\phi) \quad (41a)$$

$$E_\phi = \frac{-jk\exp(-jkr)}{2r}\sum_n \int_0^L \frac{j^{n-1}\rho_e(z_s')dz_s'}{\sqrt{1+[\rho_e'(z_s')]^2}}\left(\tilde{E}_{s\phi}I_{1n} + \tilde{E}_{s\phi}I_{2n} - \tilde{E}_{s\theta}I_{3n}\right)\exp(jkz_s\cos\theta + jn\phi) \tag{41b}$$

where

$$I_{1n} = [\rho_e'(z_s')(\cos\theta + \cos\theta') - \sin\theta']J_n'[k\rho_e(z_s')\sin\theta]$$

$$I_{2n} = -j\sin\theta J_n[k\rho_e(z_s')\sin\theta]$$

$$I_{3n} = [\rho_e'(z_s') - \sin\theta'\cos\theta + \rho_e'(z_s')\cos\theta\cos\theta']\frac{-njJ_n[k\rho_e(z_s')\sin\theta]}{k\rho_e(z_s')\sin\theta}.$$

and the well-known integral identity

$$\int_0^{2\pi}\exp(jz\cos\theta + jn\theta)d\theta = 2\pi j^n J_n(z)$$

was employed in deriving (41).

5 Sample Results

In this section, we present numerical results for three illustrative examples. The first example is a sanity-check of the developed program. By setting the dielectric constant of the radome material to 1, the computed radiation pattern is compared to that directly calculated by integrating the equivalent surface currents over the antenna's aperture. In this example, the lengths of the interior and exterior Von Karman radome surfaces are respectively $L_1 = 10\lambda_0$, $L_2 = 10.2\lambda_0$. The interior and exterior diameters at the radome base are assumed to be $D_1 = 5\lambda_0$ and $D_2 = 5.2\lambda_0$, respectively. The distance s and steering angle Ω are all set to zero. For the antenna, a circular aperture is used carrying a uniform y-polarized E-field. As shown in Figure 12, the radiation pattern of the aperture antenna through a transparent radome is in very good agreement with that from direct integration (no radome). The moment method solution is used as reference for the hybrid PO-MM and as seen the two methods are also in good agreement.

The second example shows the computed radiation pattern for the same aperture through the same radome shape and size except that the dielectric constant of the radome material is now $\epsilon_r = 2.0$. In Figure 13, we show the radiation patterns for the three different methods. The pure MM solution refers to the case when the moment method is applied everywhere on the radome's surfaces (no PO approximation is invoked); the pure PO solution refers to the

case where almost the entire surface is modeled by the physical optics currents (except for a very small region around the tip). The hybrid PO-MM solution represents the results obtained by using MM formulation up to 3λ from the tip and the rest contour currents replaced by the PO currents. Again, we observe that the hybrid solution agrees fairly well with the pure MM solution. However, the pure PO solution is substantially in error in the side lobe region. In fact, the PO result shows peaks where the MM gives nulls. The CPU time needed by these three methods for this relatively small problem is listed in the following table.

Method	CPU time (in seconds)
Pure PO	133
Pure MM	224
Hybrid PO-MM	148

The third example is that of radiation through a very large radome. The Von Karman radome is now assumed to be of length $L_1 = 100\lambda_0$ (inner), $L_2 = 102\lambda_0$ (outer); the diameters at the radome base are $D_1 = 30\lambda_0$ and $D_2 = 34\lambda_0$, respectively; and $\epsilon_r = 4.0$ for the radome material. The aperture antenna is of radius $2\lambda_0$ and a uniform y-directed field distribution is again assumed. The computed radiation patterns by the hybrid PO-MM and the pure PO are shown in Figure 14. No pure MM solution is shown due to the excessive computer resources needed to carry out this analysis. For the hybrid PO-MM solution, the MM arc was $10\lambda_0$ long from the tip and the rest was assigned to the PO-region. It should be mentioned that the CPU time for the hybrid PO-MM is about 5.5 hours.

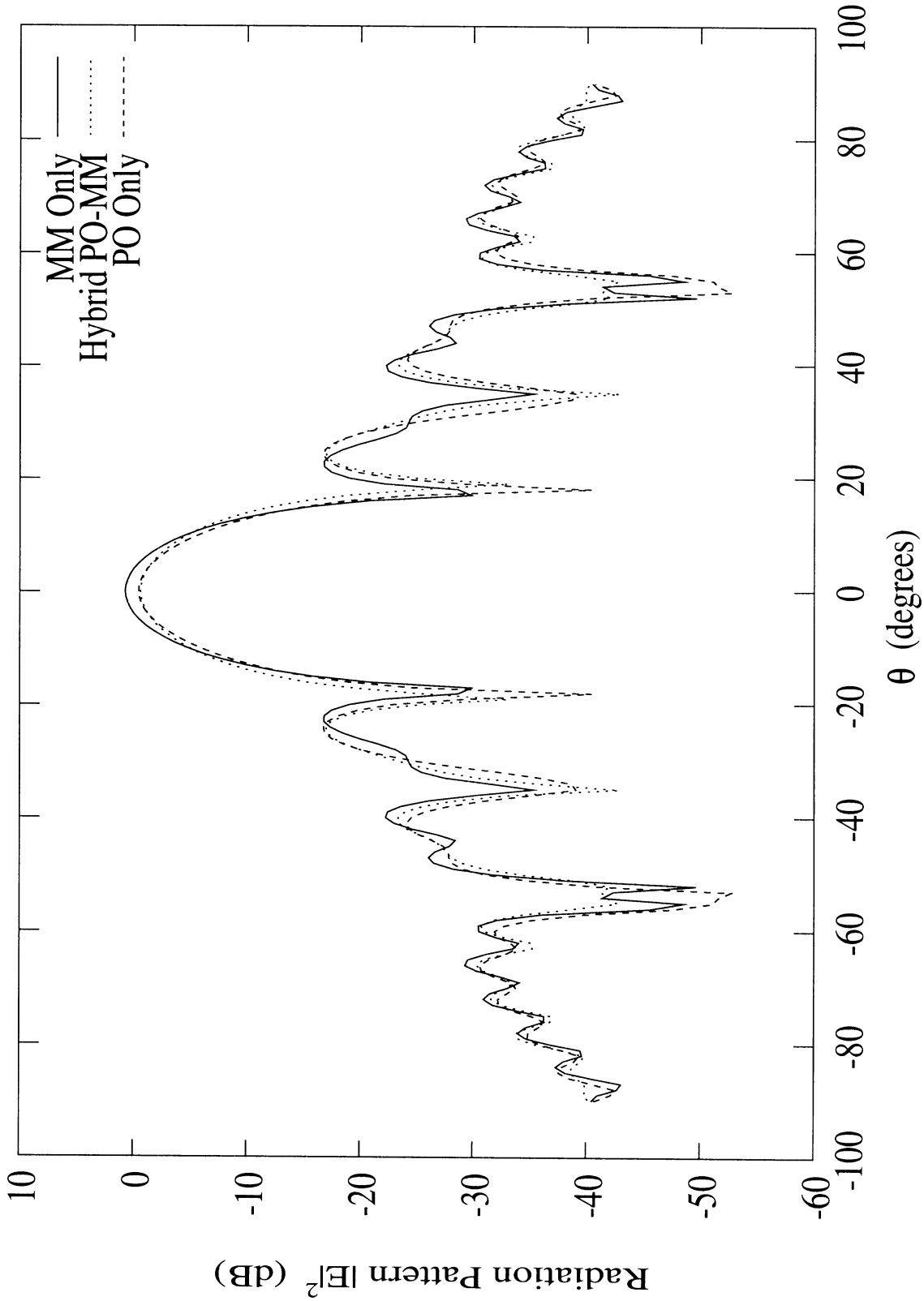

Figure 12: Comparison of computed results for the radiation pattern of an aperture through a transparent radome ($L_2 = 10.2\lambda$, $L_1 = 10\lambda$, $D_2 = 5.2\lambda$, $D_1 = 5\lambda$, $\epsilon_r = 1$).

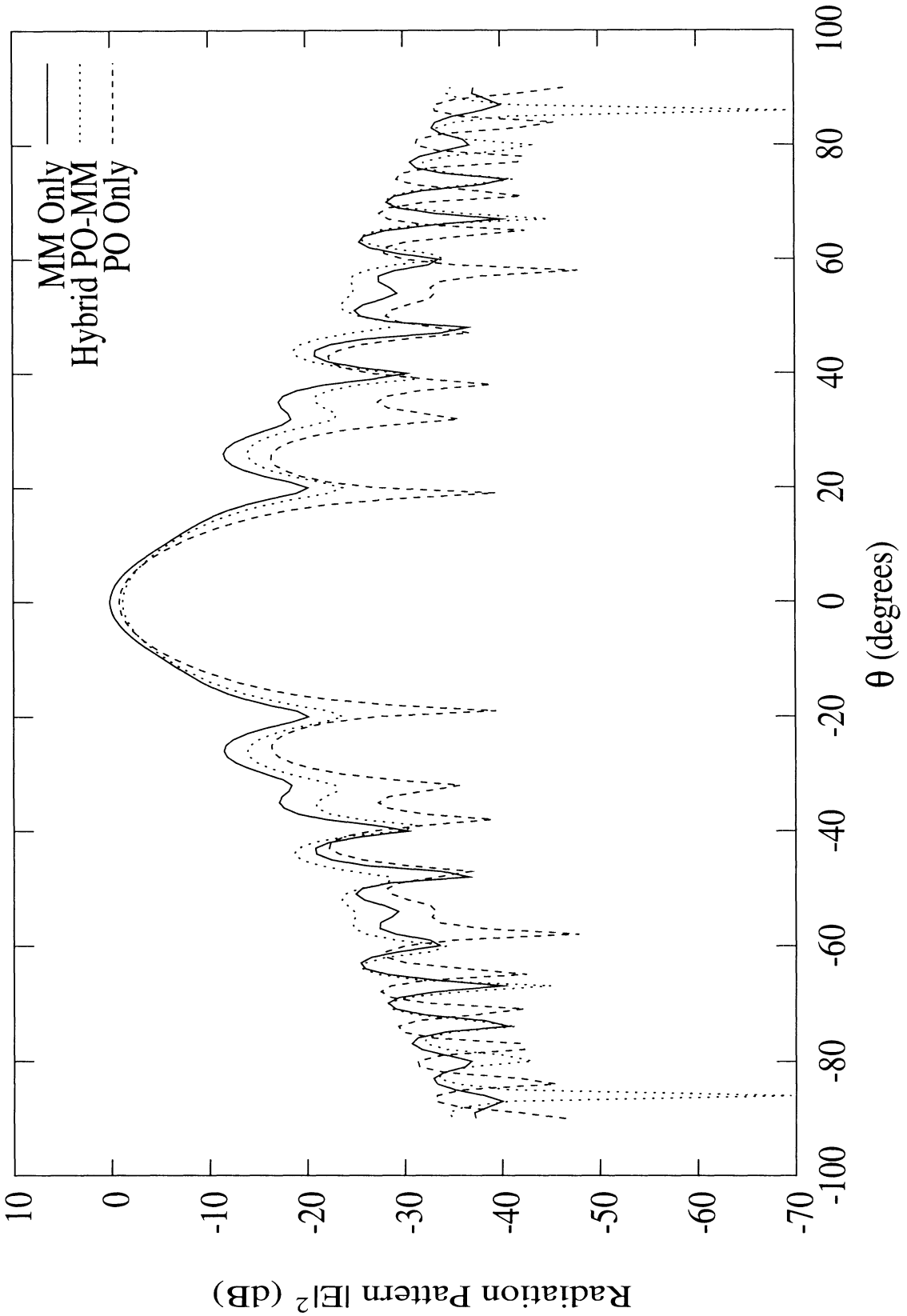

Figure 13: Radiation pattern of a radome-enclosed aperture antenna ($L_2 = 10.2\lambda$, $L_1 = 10\lambda$, $D_2 = 5.2\lambda$, $D_1 = 5\lambda$, $\epsilon_r = 2$).

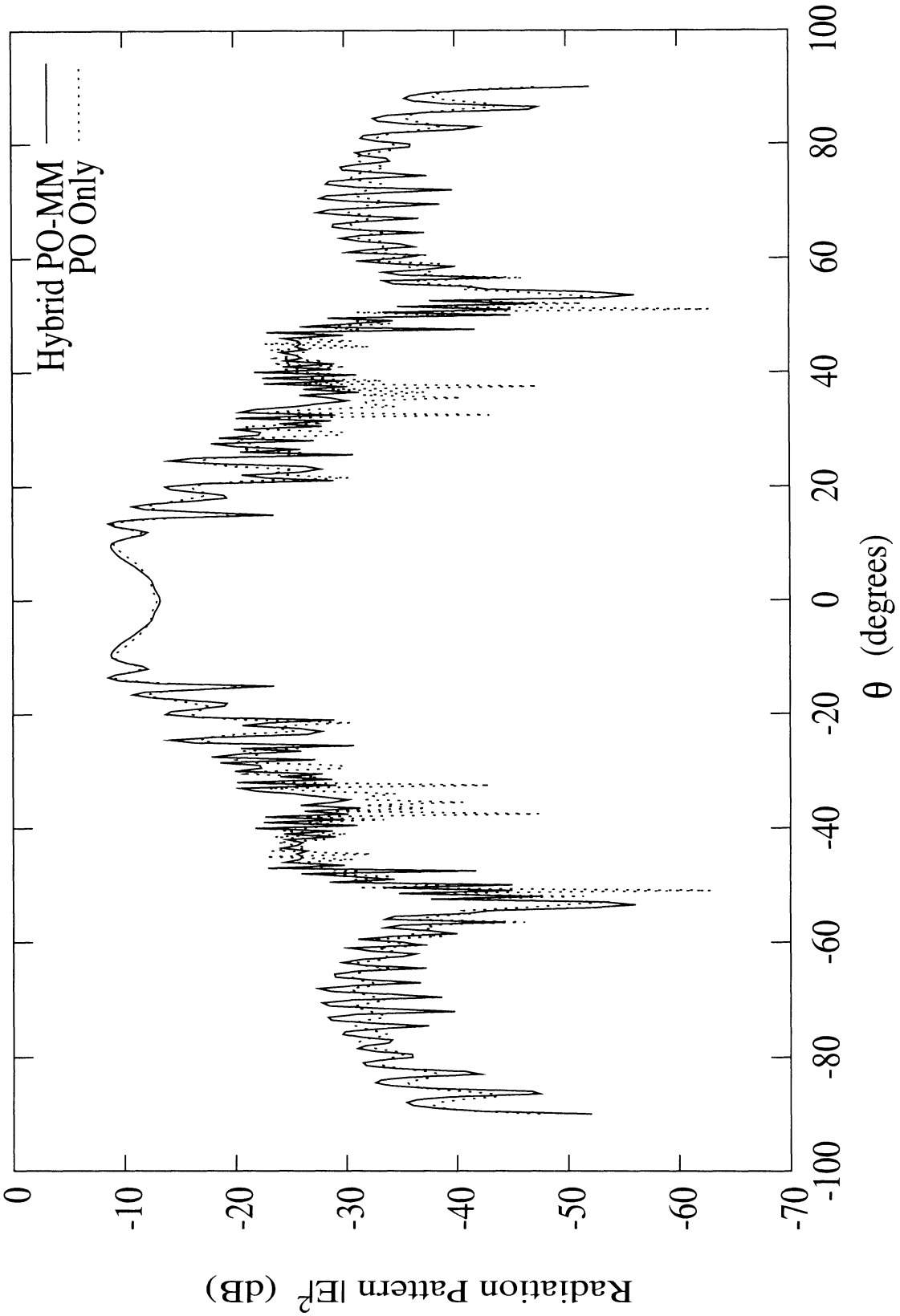

Figure 14: Radiation pattern of an aperture antenna through a very large radome ($L_2 = 102\lambda$, $L_1 = 100\lambda$, $D_2 = 34\lambda$, $D_1 = 30\lambda$, $\epsilon_r = 4$).

6 Description of ABOR, a Computer Program for Antenna Radiation Through Radomes

Our computer program for evaluating antenna radiation through radomes is called "ABOR" and can be divided into six sections. The first section of the program needs the user-provided parameters,including radome's length, diameter, shape and dielectric constant, aperture size as well as the location and orientation and field distribution on the aperture surface. The second section of the program calculates the near-zone radiated field from the antenna aperture on the insider surface of the radome. This section of the program can of course be changed by different antenna apertures. The third section of the program determines the PO equivalent surface currents on both the interior and exterior radome surfaces. Another section of the program carries out the moment method solution for the hybrid implementation and uses the antenna radiated fields and the PO currents on the radome's surfaces as excitation. The fifth program section combines all available information to calculate the far-region radiation pattern through the dielectric radome. The latter section of the program is a collection of standard subroutines, such as LU decomposition, spline interpolations for curved arcs and surfaces. The following subsections give all the six sections of the program mentioned above.

6.1 Acquiring Data

The subroutines that fulfill the task of acquiring the input data are:

- *radome_inpu*

  Subroutine *radome_inpu* gets the information pertaining the radome shape, radome length and bottom diameter, dielectric constant ϵ_r.

- *aperture_inpu*

  Subroutine *aperture_inpu* acquires the information for the aperture antenna, including the radius r_{ap} of the circular aperture, files storing the field distribution on the aperture surface, distance s, and steering angle Ω.

- *input(mode,ang,ang1,ang2,nang,npir,npor,np1o,np2o)*

  This subroutine reads-in the following parameters: mode, ang, ang1, ang2, nang, npir, npor, np1o, np2o, bk, and lmm. These variables are explained in Appendix B.

- *DBORIN*

  This subroutine calculates the required parameters such as information for the discretization of the radome arc and the basis functions based on the entered parameters.

6.2 Computing and Decomposing the Near-Zone Fields

- *subroutine nfint(r,phi,xa,ya,za,sph,cph,sth,cth,efr,eft,efp,hfr,hft,hfp)*

  Subroutine *nfint* defines the functions for all six near-zone field components (three electric components and three magnetic field components) at a given point (r, phi) for a known aperture field distribution.

- *subroutine nearfd(nip,zp,rop,some,come,fepr,fepa,fepe,fhpr,fhpa,fhpe)*

  This subroutine calculates the near-zone electric and magnetic fields.

- *subroutine ecomp(mode,npir)*

  Subroutine *ecomp* decomposes all six field components into modes and stores all the computed results into six two-dimensional array, which are called later for computing the PO fields (interior and exterior of the radome) and the MM excitation fields.

6.3 PO Currents

Subroutine *pof(n,mode,npir,npor,np1o,np2o,cfv,cfi,cfo)* calculates the PO equivalent surface currents on the interior and exterior surfaces of the radome, for a given mode.

6.4 Moment Method Solution

- *SUBROUTINE LOP*

  Subroutine *LOP(Z, ISYM, N, C, MU, EPS, NPI, RSI, ZSI, DSI, SVI, CVI, TI, TPI,*

NPJ, RSJ, ZSJ, DSJ, SVJ, CVJ, TJ, TPJ) calculates the L operator for a given boundary and a specified region.

- *SUBROUTINE KOP*

  Subroutine *KOP(Z, ISYM, N, C, MU, EPS, NPI, RSI, ZSI, DSI, SVI, CVI, TI, NPJ, RSJ, ZSJ, DSJ, SVJ, CVJ, TJ)* calculates the K operator for a given boundary and a specified region.

- *SUBROUTINE CZGEN(N,Z,Z1)*

  Subroutine *CZGEN* assembles the computed L and K operators into a matrix, which is then factorized into two triangular matrices (LU decomposition).

- *SUBROUTINE RCRGEN(N,NPIR,NPOR,NP1O,NP2O,CFV,CFI,CFO,CBR)*

  Subroutine *RCRGEN* generates the right-hand side of the hybrid matrix equations. This subroutine also calls another one named *LKOP(N, C, MU, EPS, NPI, RSI, ZSI, DSI, SVI, CVI, TI, TPI, NPJ, RSJ, ZSJ, DSJ, SVJ, CVJ, TJ, TPJ, QLTT, QLTP, QLPT, QLPP, QKTT, QKTP, QKPT, QKPP)* for the L and K operators of the PO part.

6.5 Main Program

The main program utilizes all available information and control the execution. The far-zone radiation pattern is computed at the end of the main program by calling subroutine *RCSPAT(N,NPOR,TH,RBT,RBP)*. Matrix dimension check is also done in the main program. It should be mentioned that after gathering all entered information, the main program calls a subroutine named *RECOVE(NPIR,MODE,ANG, ANG1,ANG2,NANG,rsum)* to calculate the radiation pattern directly from the field distribution on the aperture antenna.

6.6 Standard Auxiliary Subroutines

The following standard auxiliary subroutines are used in the program 'ABOR'.

- *SUBROUTINE GAUSS(WT,ASC,N,AA,BB)*

  Subroutine *GAUSS* calculates the weights and integration points of coordinates for performing Gaussian quadrature of a given order.

- *SUBROUTINE BESJ(X,N,BJM,BJ,BJP)*

  Subroutine *BESJ* computes the J_n, J_{n+1}, and J_{n+1} Bessel functions for a given argument x and order n.

- *SUBROUTINE CGECO(A,LDA,N,IPVT,RCOND,Z)*

  This standard subroutine from LINPACK does the LU decomposition for a complex matrix A. Some other similar subroutines such as *SUBROUTINE CGEFA(A, LDA, N, IPVT, INFO)* and *CGESL(A, LDA, N, IPVT, B, JOB)* are also needed to solve a linear matrix equation.

- *subroutine curv1 (n,x,y,slp1,slpn,islpsw,yp,temp,sigma,ierr)* Subroutine *curvl* determines the parameters necessary to compute an interpolatory spline under tension through a sequence of functional values. Another *function curv2 (t,n,x,y,yp,sigma)* is used to interpolates a curve at a given point using a spline under tension.

- *subroutine surf1*

  Subroutine *surf1(m, n, x, y, z, iz, zx1, zxm, zy1, zyn, zxy11, zxym1, zxy1n, zxymn, islpsw, zp, temp, sigma, ierr)* determines the parameters necessary to compute an interpolatory surface passing through a rectangular grid of functional values. A follow-up *function surf2(xx, yy, m, n, x, y, z, iz, zp, sigma)* interpolates a surface at a given coordinate pair using a bi-spline under tension.

- *Functions bessjd(n,x) and BESSJ(N,X)*

  These two functions calculate the Bessel $J_n(x)$ and its derivative $J_n'(x)$ using double precision.

7 Running the Program ABOR (ABOR Manual)

The program ABOR consists of two parts: ABOR.f and ABOR_SUBS.f. On unix, one can use the command

f77 -o ABOR ABOR.f ABOR_SUBS.f -O

for compiling, or just simply type

make

to generate the executable file "ABOR". A detailed description of the input data required to execute ABOR is given below. The definition of each input variable is also provided.

- read(*,*) BK

  ——————————- Input the free-space wave number $(2\pi/\lambda)$

- read(*,*) MODE

  ——————————- Read number of modes considered. The recommended number of modes is the closest integer to $k\rho_{max} + 1$.

- read(*,*)IRS

  ——————————- Specify the radome shape

  $IRS = 1$, *for Von Karman Radome*

  $IRS = 2$, *for Radome shape defined by the user as data files.*

- Read(*,*) L_1, D_1, L_2, D_2, and s if $IRS = 1$

  ——————————- Give values of Von Karman radome's interior length, interior diameter, exterior length, exterior diameter, and shift s along the z-axis.

- Read(*,*) radin.dat if $IRS = 2$

  ——————————- Input the file name storing the interior curve of the dielectric radome (see 7.2 for definition of format).

- Read(*,*) radout.dat if $IRS = 2$

  ——————————- Input the file name storing the exterior curve of the dielectric radome (see 7.2 for definition of format).

- Read(*,*) real(Er), imag(Er)

  ——————————- Read the real and imaginary parts of the complex dielectric constant of the radome material.

- Read(*,*) Lmm

  ——————————- Read the length along the z-axis defining the radome arc over which moment method will be performed.

- Read(*,*) Phi

  ——————————- Define the ϕ angle (in degrees) at which the radiation pattern will be computed.

- Read(*,*) Ang1, Ang2, Nang

  ——————————- Input the starting angle and stop angle (in degrees) of θ and the number of sampling points between Ang_1 and Ang_2.

- Read(*,*) Omega

  ——————————- Define the angle Ω for antenna's rotated direction.

- Read(*,*) Rapa, Rsubr, Nrad, Nphi

  ——————————- Read the radius of the circular aperture antenna, radius of the circular sub-reflector, number of sampling points in the radial direction, number of sampling points in the azimuthal direction.

- Read(*,*) Ex.dat

  ——————————- Input the name of the data file for reading the x component of electric field on the aperture surface (see section 7.3 for definition of data file format).

- Read(*,*) Ey.dat

  ——————————- Input the name of the data file for reading the y component of electric field on the aperture surface (see section 7.3 for definition of data file format).

To familiarize the user with the input data file, two sample data files are given in Subsection 7.1. Subsection 7.2 demonstrate the structure of the data file defining the radome shape. Subsection 7.3 details the structure of the data files storing the aperture E-field distribution.

7.1 Sample Input Date Files

This appendix gives two examples for the input data file. The first is for a Von Karman radome, and the other is for a radome specified by the user.

Example One: Von Karman Radome

6.2832

5

1

15.0, 5.0, 16.0, 6.0, 0.0

2.2, 0.0

3.0

0.0

0., 90., 91

0.0

2., 20, 20

Ex.dat

Ey.dat

Example Two: User-Defined Radome

6.2832

5, 0.5

2

radin.dat

radou.dat

2.2, 0.0

3.0

0.0

0., 90., 91

0.0

2., 20, 20

Ex.dat

Ey.dat

7.2 Sample Data File for Defining the Radome's Shape

This subsection gives a sample data file for defining the radome's interior and exterior surface. Both interior and exterior use the same data structure. The number of sampling points will be determined by the program from this input data file. Sampling points can be non-uniformly distributed over the radome arc.

z	$\rho(z)$
.0000000	1.5000000
.5000000	1.4859140
1.0000000	1.4604454
1.5000000	1.4277130
2.0000000	1.3891178
2.5000000	1.3454080
3.0000000	1.2970309
3.5000000	1.2442598
4.0000000	1.1872478
4.5000000	1.1260552
5.0000000	1.0606601
5.5000000	.9909589
6.0000000	.9167565
6.5000000	.8377454
7.0000000	.7534657
7.5000000	.6632326
8.0000000	.5659961
8.5000000	.4600385
9.0000000	.3421973
9.5000000	.2050837
10.0000000	.0000000

7.3 Data File Storing the Aperture Field Distribution

This subsection provides a sample data file for storing values of the electric field components on the aperture surface. Both x- and y-directed components have the same data structure and the same sampling points. For the example considered here, we assume $N_{rad} = 4$ and $N_{phi} = 6$. The location of these sampling points is shown in Fig. 15.

(1.0, 0.0)

(1.0, 0.0)

(1.0, 0.0)

(1.0, 0.0)

(1.0, 0.0)

(1.0, 0.0)

(1.0, 0.0)

(1.0, 0.0)

(1.0, 0.0)

(1.0, 0.0)

(1.0, 0.0)

(1.0, 0.0)

(1.0, 0.0)

(1.0, 0.0)

(1.0, 0.0)

(1.0, 0.0)

(1.0, 0.0)

(1.0, 0.0)

(1.0, 0.0)

(1.0, 0.0)

(1.0, 0.0)

(1.0, 0.0)

(1.0, 0.0)

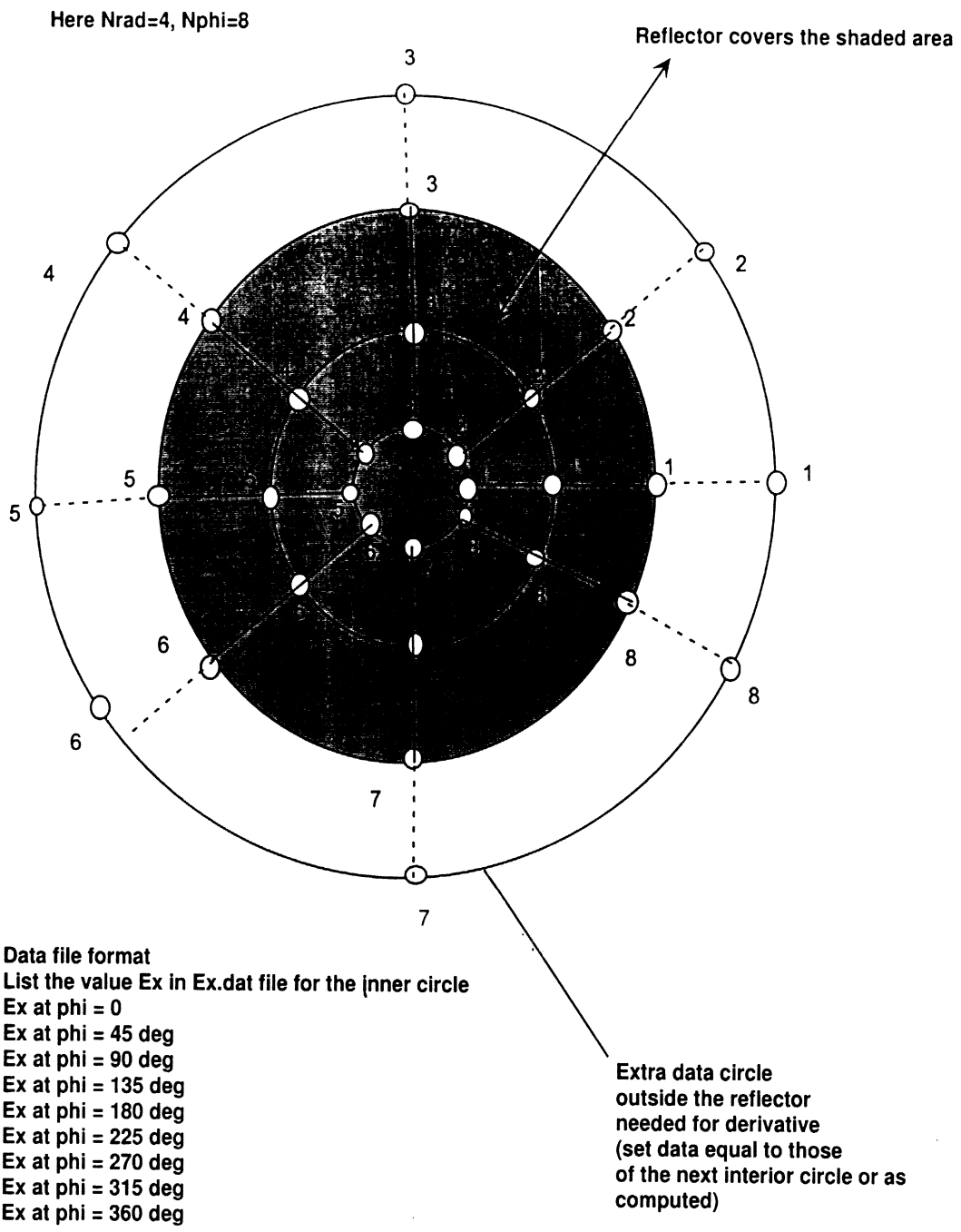

Figure 15: Von Karman Radome

8 Appendix A: Von Karman Radome

The governing equation for the Von Karman radome is

$$\rho(z) = \frac{D}{2\sqrt{\pi}}[\Phi - 0.5\sin(2\Phi)]^{1/2} \qquad (A1)$$

where

$$\Phi = \cos^{-1}(\frac{2z}{L} - 1).$$

Differentiating (A1) gives

$$\rho'(z) = \frac{-D\sin\Phi}{\sqrt{\pi}L\sqrt{\Phi - 0.5\sin(2\Phi)}} \qquad (A2)$$

A typical Von Karman radome is shown in Figure 16.

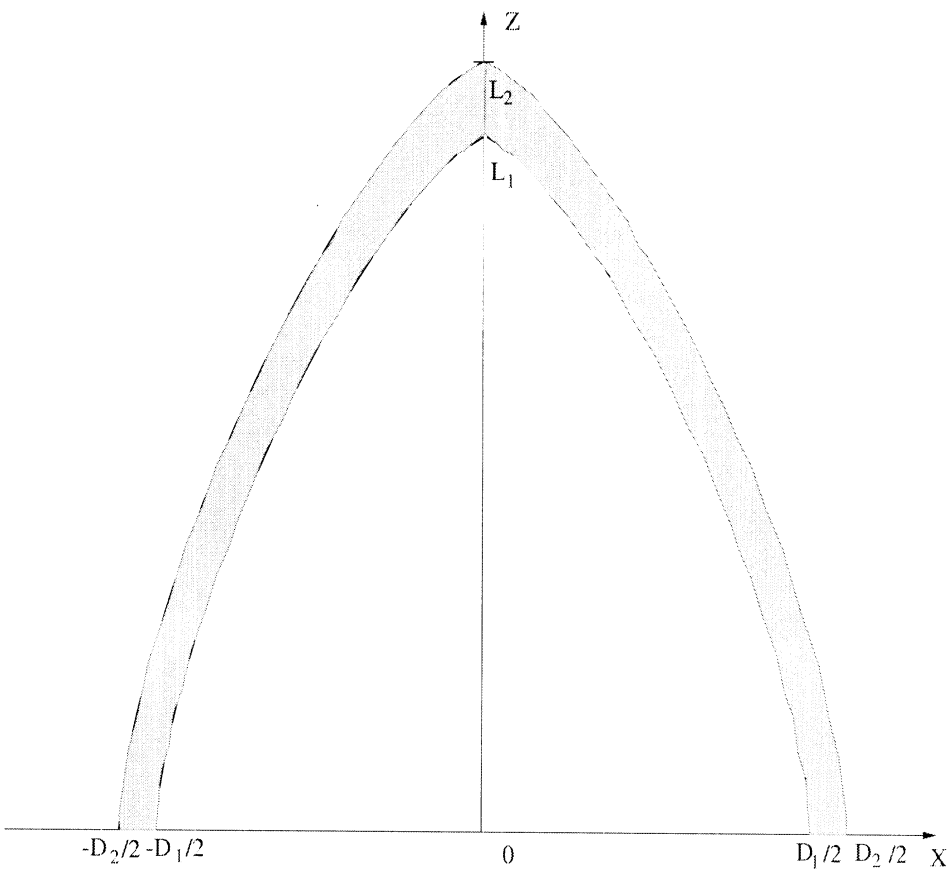

Figure 16: Von Karman Radome

9 Appendix B: Input Variables Description

ANG	Fixed ϕ angle (degrees).
ANG1	Starting θ angle (degrees).
ANG2	Stop θ angle (degrees).
BK	Wave number ($2\pi/\lambda_0$ for the problem (meters^{-1}).
D_1	Diameter of the interior bottom surface.
D_2	Diameter of the exterior bottom surface.
Er	Dielectric constant of the radome material.
Ex.dat	File name that stores the x-component of E-field over antenna aperture.
Ey.dat	File name that stores the y-component of E-field over antenna aperture.
IRS	Index for radome shape. IRS=1 for Von Karman radome; IRS=2 for radome shape defined by the user as data files.
L_1	Length of the interior radome surface.
L_2	Length of the exterior radome surface.
Mode	Number of modes considered. Maximum number can be set to $k\rho_{max} + 1$.
NANG	Number of varied θ angles.
NPIR	Number of sampling points on radome's interior surface.
NPOR	Number of sampling points on radome's exterior surface.
NP1O	Number of Sampling points for the PO-part on the interior surface.
NP2O	Number of Sampling points for the PO-part on the exterior surface.

N_{phi}	Number of sampling points in the azimuthal direction for aperture field distribution.
N_{rad}	Number of sampling points in the radial direction for aperture field distribution.
radin.dat	File name storing the interior curve of the radome (IRS=2).
radou.dat	File name storing the exterior curve of the radome (IRS=2).
R_{apa}	Radius of the circular aperture antenna.
R_{subr}	Radius of the circular sub-reflector.
s	Distance from radome's bottom center to antenna's location (meters).
Ω	Steering angle of the antenna (degrees).

10 Appendix C: Optimizing parameters for speeding up the Axi-Symmetric Body of Revolution (ABOR) code

Introduction The Axi-Symmetric Body of Revolution (ABOR) code used the new hybrid physical optics-moment method for analysing nose-radome antennas. The code demonstrated excellent accuracy and speed for radomes of large length as 100λ with an aperture antenna of radius of 2λ. Motivated by the trials to run the code for such large radomes with large apertures of $23\lambda radius$ extensive work were done to optimize the code so that accurate results are produced in a reasonable amount of time. The purpose of this report is to present the different optimizing parameters for the code and show how can these parameters be used for different kinds of problems.

In the first part of this appendix the blockage effect of the antenna subreflector is introduced. In the second part the parameters governing the speed and the accuracy of the code are investigated. We spent quite a lot of time in investigating these parameters. We ran diffirent radome geometries combined with different aperture andblockage sizes. We have concluded the optimum parameters settings for a large radome with a large aperture.

Aperture Blockage

The antenna subreflector blockage was implemented in the code by altering the integration interval over the aperture. Instead of integrating from 0 to r_{ap} , the integration now is now modified to be from r_{subr} (the sub-reflector radius) to r_{ap} (the aperture radius). The aperture subreflector radius should be entered in the input file after the apperture radius. The old format was Rapa, Nrad, Nphi. The new make file the format of this line should be Rapa, Rsubr, Nrad, Nphi. Explicitly

Old Format: Read(*,*) Rapa,Nrad, Nphi

New Format: Read(*,*) Rapa, Rsubr, Nrad, Nphi

Fig. 17 shows the results of the farfield pattern for the exact solution and that generated by the modified code. As seen the agreement between the modified ABOR code and the exact solution is excellent. The exact solution for a constant X-directed aperture field is given by

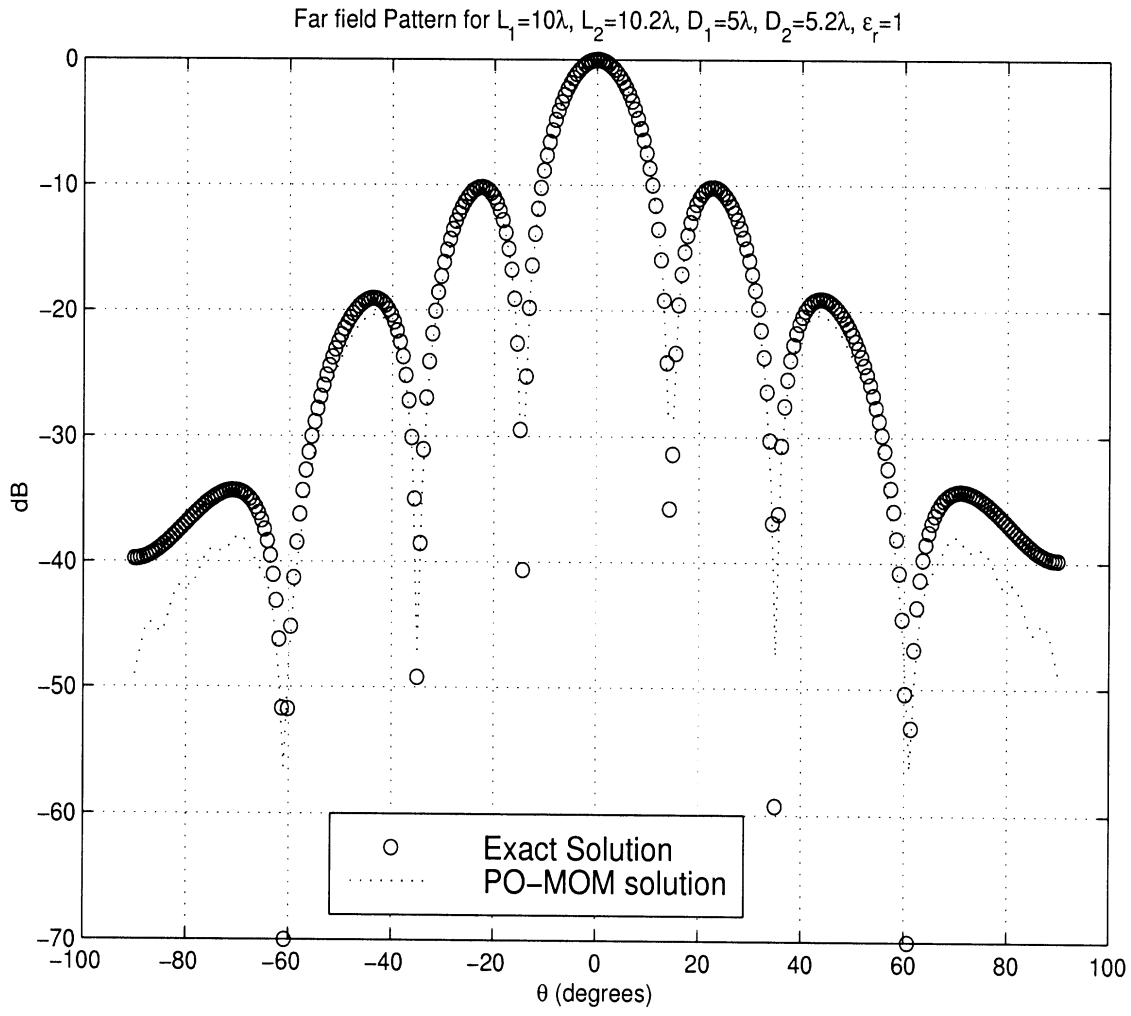

Figure 17: Exact solution and the farfield pattern through a radome with $\epsilon_r = 1$

$$E(r) = f(t)\left[\cos\phi\ \hat{\theta} - \sin\phi\cos\theta\ \hat{\phi}\right] \tag{1}$$

$$f(t) = \frac{a^2 J_1(ak_0\sin\theta)}{k_0 a\sin\theta} - \frac{b^2 J_1(bk_0\sin\theta)}{k_0 b\sin\theta} \tag{2}$$

where a is the main reflector radius, b is the subreflector radius, k_0 is the free space wave number, J_1 is the Bessel function of the first kind and of order one, and θ and ϕ are the spherical coordinates.

Parameter Optimization for speeding up the code:

The parameters that can be varied to speed up the code are:

1. **NGUASS:** number of Gaussian integration points used between sampled points on the aperture. Fig. 18 shows the results for **Ngauss** = 2,3 and 4. It can be concluded that **NGAUSS** can not be degraded when integrating over the aperture as it will severely affect the accuracy of the solution.

2. **NPIR:** number of sampling points used on the radome's internal surface.
   NPOR: number of sampling points used on the radome's outersurface.
   The formaulas for calculating **NPIR** and **NPOR** in the code are:
   NPIR=nint(**FACTOR***15*tl1*bk/6.2831)+1
   NPOR=nint(**FACTOR***15*tl2*bk/6.2831)+1
   Fig. 19 shows the results for different values of **FACTOR** when $L_1 = 100\lambda$, $L_2 = 100\lambda$, $D_1 = 30\lambda$, $D_2 = 30\lambda$ and $\epsilon = 4$. This parameter is a key to speed up the code. Table 1 shows the CPU time and the corresponding factor value for the **NPIR** and **NPOR**. From these results it can be concluded that the optimum value for this factor is 7/15.

   Let us now consider a much larger reflector. For a large radome ($L_1 = 100\lambda$, $L_2 = 102\lambda$, $D_1 = 60\lambda$, $D_2 = 63\lambda$), but with much lareger reflector $R_{apr} = 23\lambda$. The corresponding pattern for $\epsilon_r = 1$ and $R_{subr} = 0$ is given in Fig. 20. Since ϵ_r is unity, itis expected that this pattern will gree with the analytical integration. It is clear that in spite of the CPU time reduction from 20 days (estimated) down to 54 hours and 43 minutes, the accuracy

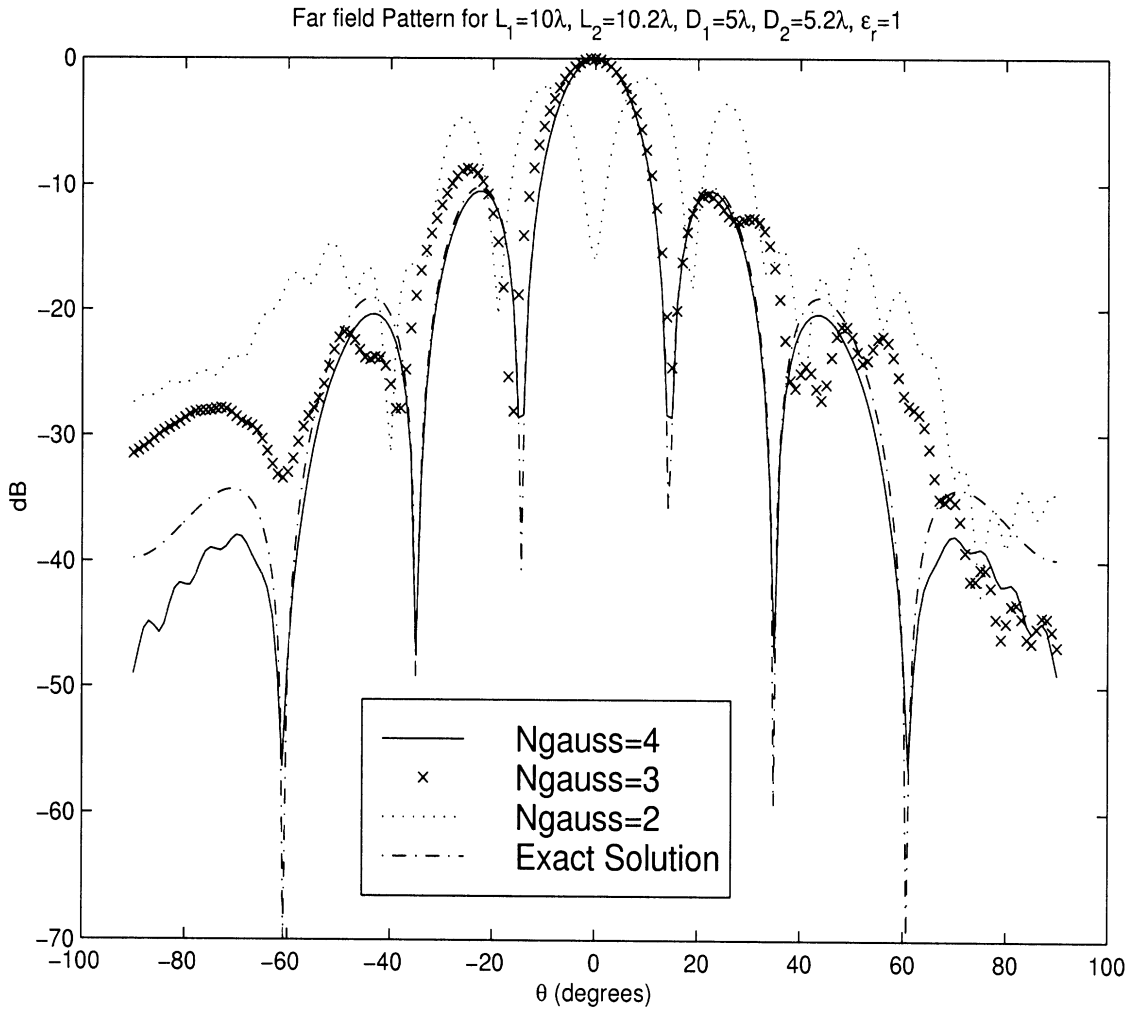

Figure 18: Results for different npir and npor values

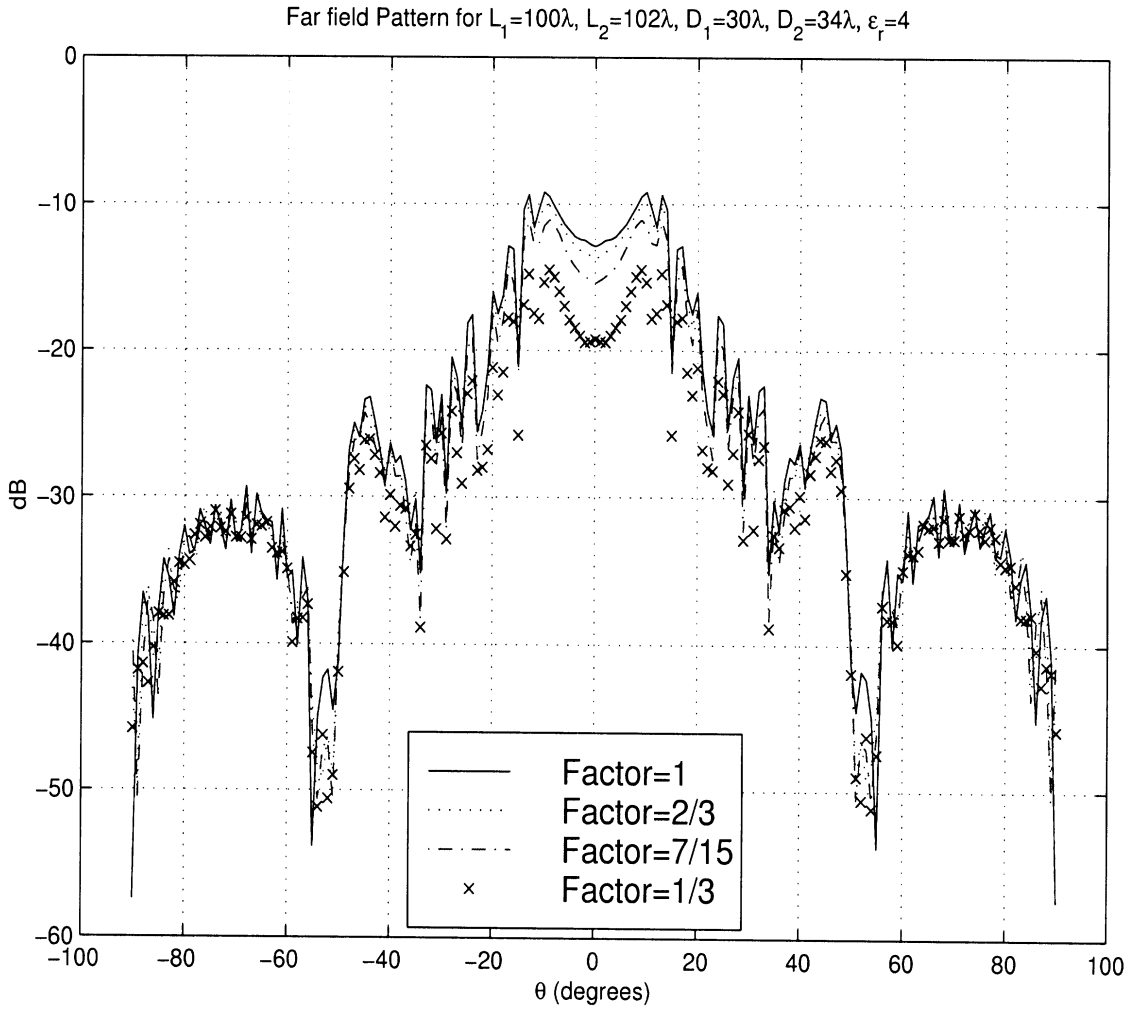

Figure 19: Results for different npir and npor values

Factor	CPU time
1	10 hours and 47 minutes
2/3	5 hours and 56 minutes
7/15	3 hours and 16 minutes
1/3	1 hour and 52 minutes

Table 1: Values for the npir factor and the corresponding CPU time

of the main and side lobe levels is unacceptabl. This is revealed more in Fig. 21 where we see that the main lobe is $6db$ down. the

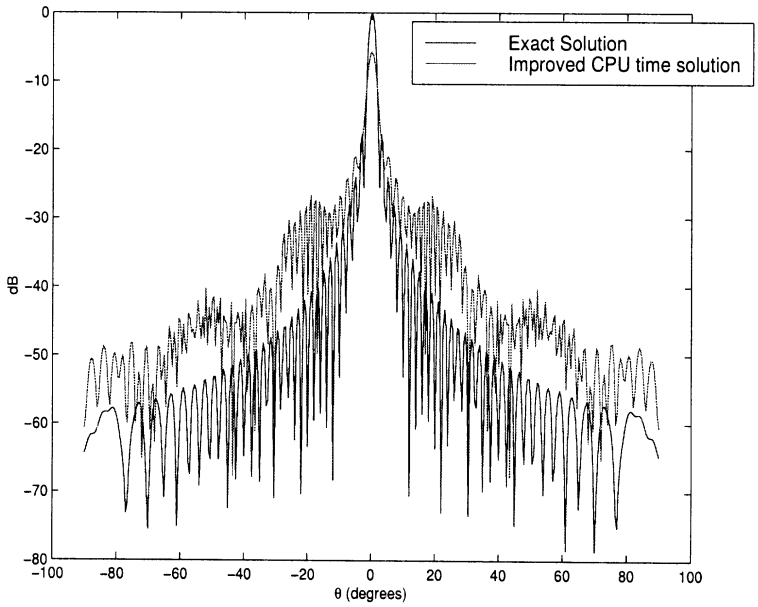

Figure 20: Results for the large radome with large reflector with the parameter factor=7/15

So this optmization parameter **FACTOR** can not be used alone for a large radome with a large reflector.

3. **NR:** number of integration pointson the aperture.Fig. 22 shows the results for a small apperture.Table 2 shows the nr values and the corresponding CPU time. It can be observed that for a small radome and a small aperture, **NR** makes a great difference. However, for a large radome and a small aperture the reduction in cpu time is negligable. The effect of **NR** on a large radome with a large aperture is expected to be significant (It will be demonstrated later).

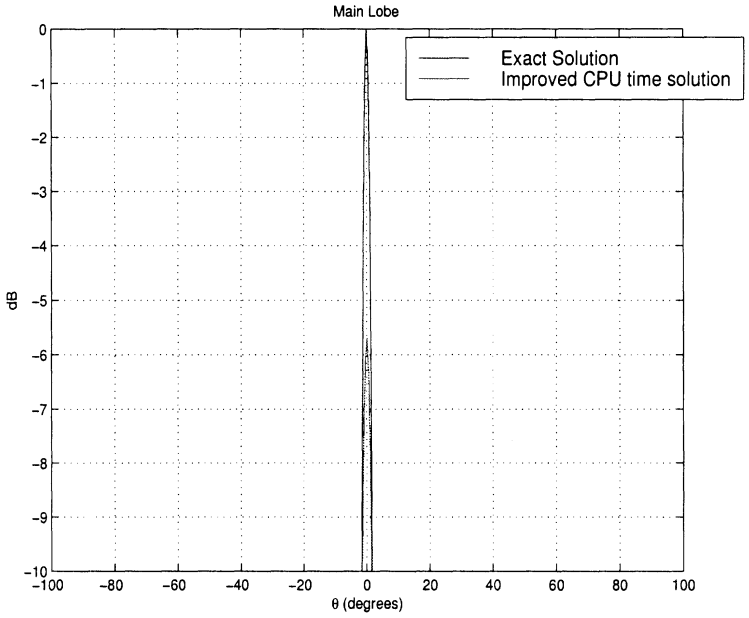

Figure 21: Results for the main beam with the parameter factor=7/15

nr	CPU time
7	10 minutes
4	6 minutes
3	3 minutes

Table 2: Values for nr and the corresponding CPU time

4. **NIP**,number of integration point from 0 to 2π for modal decomposition. Setting **NIP** to 10 and **Factor** to 10/15 gives exact results and CPU time of 26 hours and 12 minutes the results are shown in Fig. 23.

   The combined effect of **NIP**, **NPIR,NPOR** and **NR** is now considered where **NIP** is set to 10, **Factor** is set to 2/3 and **NR** is set to 15 points instead of 60 points. This will lead to a CPU time of 26 hours. Fig. 24 shows the results which is in excellent agreement with the far field pattern.Table 3 shows the values for **NIP** and **NR** and the corresponding CPU time. It should be noted that the reduction of the **NR** points will work fine with apertures that have no rapid tapering. In case of field tapering **NIP** and **Factor** are the only parameters to be optimized.

Conclussion After the detailed study of optimizing the various parameters for speeding up

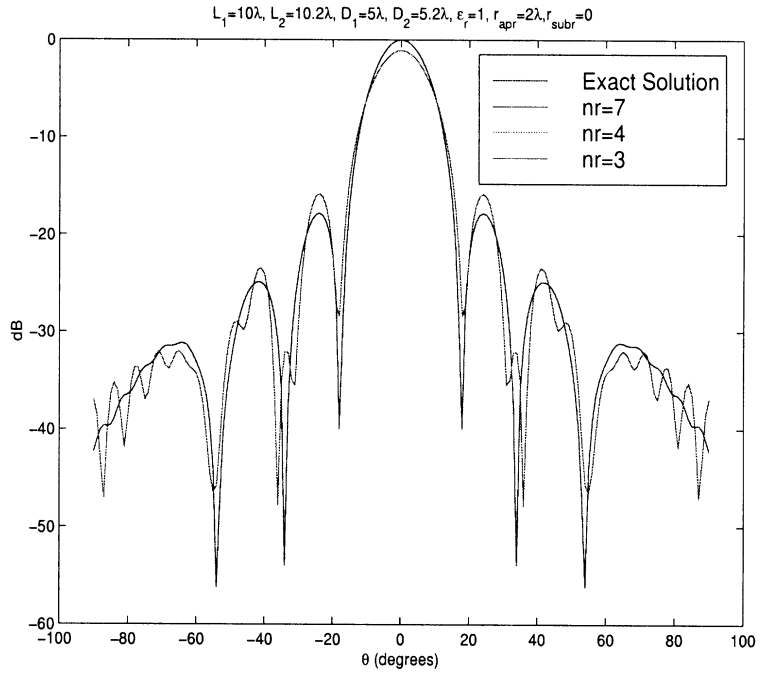

Figure 22: Results nr=7,4 and 3

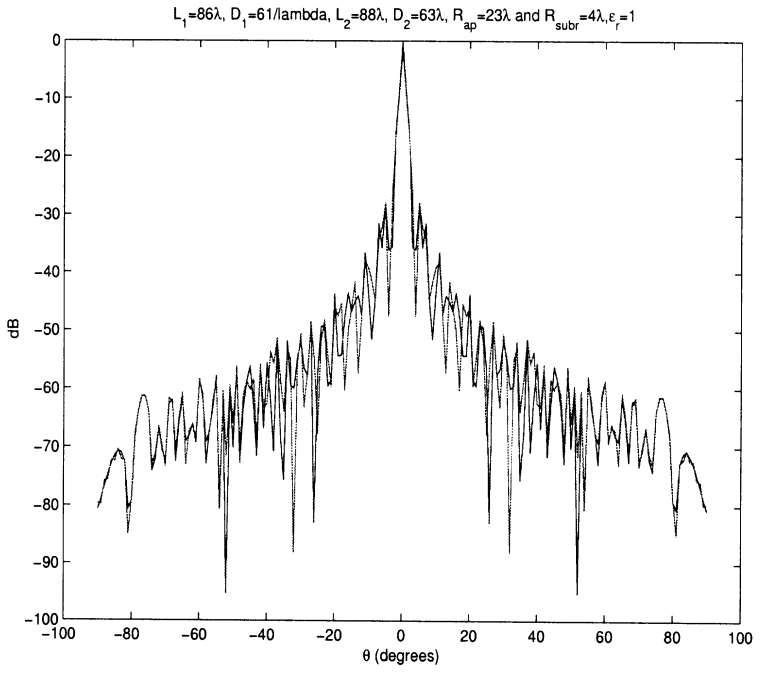

Figure 23: Results for **NIP=10** and **Factor=10/15**

the ABOR code, we conclude the following recomended values:

NIP = 10

FACTOR = 10/15

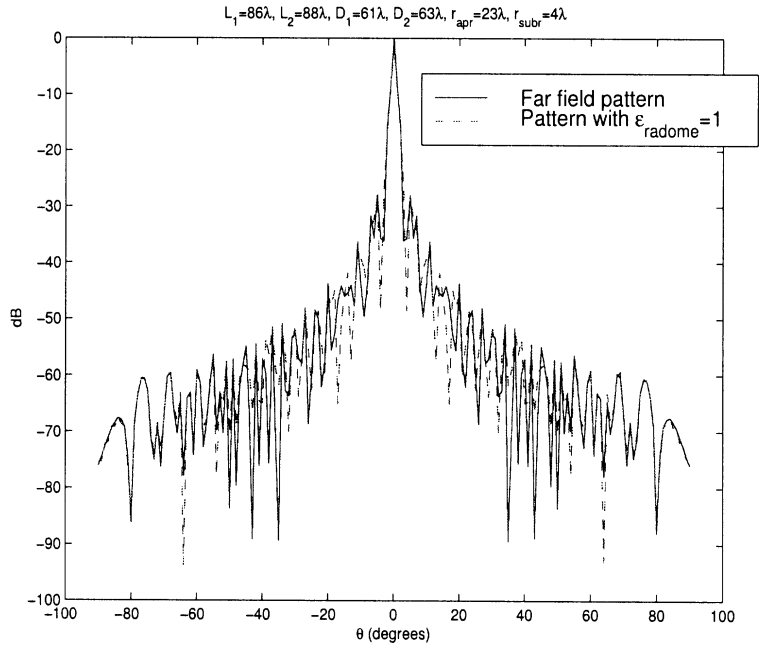

Figure 24: Results for **NIP**=10, **Factor**=10 and **NR**=15 points

nip	nr	CPU time
10	60	26 hours and 7 minutes
10	15	7 hours and 30 minutes

Table 3: Values for nip, nr and the corresponding CPU time

For constant aperture fields and slow tapered aperture fields an extra reduction in CPU time is achieved by reducing **NR** by a factor of 4.

References

[1] L.N. Medgyesi-Mitschang and J.M. Petnam, "Combined field integral equation formulation for axially inhomogeneous bodies of revolution," MDC Report, 1988.

[2] J.R. Mautz and R.F. Harrington, "H-field, E-field, and combined field solution for bodies of revolution," *Interim Technical Report*, RADC-TR-77-109, March 1977.

[3] A.W. Glisson and D.R. Wilton, "Simple and efficient numerical techniques for 3 bodies of revolution," *Technical Report No. 105*, The University of Mississippi, March 1979.

[4] J.R. Mautz and R.F. Harrington, "H-field, E-field, and combined-field solutions for conducting bodies of revolution," *Arch. Elek. Ubertragung.,* vol.32, pp.157-164, 1978.

[5] J.R. Mautz and R.F. Harrington, "Electromagnetic scattering from a homogeneous material body of revolution," *Arch. Elek. Ubertragung.,* vol.33, pp.71-80, 1979.

[6] L.N. Medgyesi-Mitschang and J.M. Putnam, "Electromagnetic scattering from axially inhomogeneous bodies of revolution," *IEEE Trans. Antennas and Propagat.*, vol. AP-32, no.8, pp.797-806, 1984.

[7] K. Umashankar, A. Taflove, and S.M. Rao, "Electromagnetic scattering by arbitrary shaped three-dimensional homogeneous lossy dielectric objects," *IEEE Trans. Antennas and Propagat.*, vol. AP-34, no.6, pp.758-766, 1986.

[8] P.L. Huddleston, L.N. Medgyesi-Mitschang, and J.M. Putnam, "Combined field integral equation formulation for scattering by dielectrically coated conducting bodies," *IEEE Trans. Antennas and Propagat.*, vol. AP-34, no.4, pp.510-520, 1986.